

**STUDY OF A NOVEL NANOCRYSTALLINE MATERIAL: MODELING THE SCALING
EFFECTS OF TOROIDAL TRANSFORMERS UTILIZING ANSYS MAXWELL AND
EXAMINING THE POWER DENSITY OF INDUCTION MOTORS UTILIZING ANSYS
RMXPRT**

by

Oreste V. Scioscia Jr.

Bachelor of Science in Mechanical Engineering, University of Pittsburgh, 2011

Submitted to the Graduate Faculty of
Swanson School of Engineering in partial fulfillment
of the requirements for the degree of
Master of Science

University of Pittsburgh

2013

UNIVERSITY OF PITTSBURGH
SWANSON SCHOOL OF ENGINEERING

This thesis was presented

by

Oreste V. Scioscia Jr.

It was defended on

November 5, 2013

and approved by

Zhi-Hong Mao, PhD, Associate Professor, Electrical and Computer Engineering Department

TomMcDermott, PhD, Assistant Professor, Electrical and Computer Engineering Department

Thesis Advisor: Gregory F Reed, PhD, Associate Professor, Electrical and Computer

Engineering Department

Copyright © by Oreste V. Scioscia Jr.

2013

**STUDY OF A NOVEL NANOCRYSTALLINE MATERIAL: MODELING THE
SCALING EFFECTS OF TOROIDAL TRANSFORMERS UTILIZING ANSYS
MAXWELL AND EXAMINING THE POWER DENSITY OF INDUCTION MOTORS
UTILIZING ANSYS RMXprt**

Oreste V. Scioscia Jr., M.S.

University of Pittsburgh, 2013

Recent DOE reports convey the need for the advancement of soft magnetic materials for applications in high frequency, medium voltage, MW scale power electronics and grid integration technology. The soft magnetics used in these power electronics can occupy significant space, require extensive cooling, and limit designs. Operation at higher frequencies allows for reductions in converter size and weight. Nanocomposites combine the soft magnetic strengths of amorphous core materials with the more attractive saturation inductions of crystalline metals – a combination naturally well suited for high frequency converter applications.

Combinations of compositional additions and novel processing techniques have produced nanocomposites with permeability, $\mu > 10^5$, saturation induction, $B_s > 1.6\text{T}$, resistivity, $\rho > 150\mu\Omega\text{-cm}$, thickness, $t < 15\mu\text{m}$, temperature stability up to 300°C , and overall core losses less than 20W/kg at 10kHzT . The kHzT is a unit convention set by the Advanced Research Project Agency – Energy (ARPA-E).

The operation of power converters at higher frequencies is limited by increased losses in this regime, a trend accounted for by the Steinmetz Equation, (1), which relates the operating frequency, f , and saturation induction, B , to power loss.

$$P_L = 2f^\alpha B^\beta \quad (1)$$

In this equation the material dependent, empirically determined Steinmetz coefficients, $\alpha(\sim 2)$ and $\beta(\sim 1-2)$, accounts for all core losses, in which hysteretic and anomalous and conventional eddy currents losses are predominant. Noncore winding losses and switching losses in the semiconductor components compound these core losses. The operating frequency of a transformer is determined by optimizing the size reductions while taking into account the increase in losses at higher frequencies.

This research focuses on the prediction of Steinmetz coefficients of nanocomposite-based magnetic materials, using ANSYS to simulate high frequency operation. Subsequently, this research investigates the scaling effects between bench top toroidal transformers of various sizes and geometries using simulation and experimental results. A study is also performed to analyze how nanocomposites can be used in induction motor stator cores to increase power density.

TABLE OF CONTENTS

ACKNOWLEDGMENTS	XIV
1.0 INTRODUCTION.....	1
2.0 BACKGROUND	3
2.1 PURSUIT OF HIGH SWITCHING FREQUENCIES	3
2.2 A BRIEF EXPLANATION OF HIGH-FREQUENCY SWITCHING, SIZE REDUCTION, AND MATERIAL PROPERTIES	4
2.2.1 Faraday’s Law	4
2.2.2 Steinmetz Equations and Core Loss	4
2.2.3 Winding Loss – Skin and Proximity Effects	5
2.2.4 Core Loss, Winding Loss, and Permeability	6
2.3 ARPA-E MATERIAL – A NOVEL MATERIAL AND IMPLICATIONS ...	6
2.4 PROCESS FOR VALIDATING AND UTILIZING ANSYS MAXWELL....	7
3.0 CORE MODELING	9
3.1 EXPERIMENTAL TOROID DATA	9
3.1.1 Geometry	9
3.1.1.1 Flux crowding.....	10
3.1.2 Experimental Core Loss Data	11
3.2 METHODS OF ANSYS MODELING.....	16

3.2.1	Introduction	16
3.2.2	Modeling with Grouped Conductors	18
3.2.2.1	The need for high form factor.....	18
3.2.2.2	Air Gap Considerations.....	19
3.2.3	Modeling with Individual Conductors.....	20
3.3	ANSYS MODELING OF THE CORE	21
3.3.1	Introduction	21
3.3.2	Imputing Material Data	21
3.3.3	Building the Models.....	24
3.3.3.1	Introduction.....	24
3.3.3.2	Geometry Models	25
3.3.3.3	Conductor Types	26
3.3.3.4	Applying Excitations.....	28
3.3.4	Understanding the Data and Results	28
3.4	COMPARING EXPERIMENTAL AND SIMULATED RESULTS	32
3.4.1	Analyzing the Results and Observing Error	32
3.4.2	Conclusions.....	33
4.0	MOTOR MODELING	34
4.1	INTRODUCTION	34
4.2	METHOD OF TESTING.....	34
4.3	A BRIEF EXPLANATION OF MOTOR FUNDAMENTALS.....	35
4.3.1	Rotation Speed and the Number of Poles	37
4.3.2	Magnetizing Current, Flux, and the Number of Poles.....	37

4.3.3	Core (Iron) Losses	40
4.4	ROTOR MATERIAL FOR TESTS	40
4.5	NEW DATA FOR HTX-012B	42
4.6	2 POLE VERSUS 16 POLE MOTOR TEST	43
4.6.1	2 Pole Test.....	43
4.6.2	16 Pole Test.....	45
4.6.3	Results of 2 Pole versus 16 Pole Test.....	47
4.7	2 POLE VERSUS 8 POLE MOTOR TEST	53
4.7.1	2 Pole Test.....	53
4.7.2	8 Pole Test.....	55
4.7.3	Results of 2 Pole versus 8 Pole Test.....	56
4.8	CONCLUSIONS	62
5.0	FUTURE WORK	63
	BIBLIOGRAPHY	64

LIST OF TABLES

Table 1. Core Sizes and Geometries	10
Table 2. Core Loss for Annealed, Impregnated, and Impregnated and Cut Cores	12
Table 3. Permeability of Annealed, Impregnated, and Impregnated and Cut Cores	15
Table 4. Steinmetz Coefficients for Experimental Cores	16
Table 5. Study of Spacing among Layers and Quantification of Errors at 100 kHz [26].....	19
Table 6. Loss vs. Frequency Data for Solid Medium Core – 20 kHz to 100 kHz	23
Table 7. Core Loss Coefficients for Solid Medium Core	24
Table 8. Frequency and Skin Depth.....	27
Table 9. Frequency and Current Range	28
Table 10. Core Loss (mW) for Small Solid Core	29
Table 11. Experimental and Simulated Results for α and β with Error	32
Table 12. Material Data for M600-50A.....	41
Table 13. Loss vs. Frequency Data for Solid Medium Core -- 1 kHz to 20 kHz	43
Table 14. Values for Rotor and Stator Geometries of 24 Pole (Original) Motor	44
Table 15. Values for Rotor and Stator Slot Geometries of 24 Pole (Original) Motor	44
Table 16. Values for Rotor and Stator Geometries of 16 Pole Motor	45
Table 17. Values for Rotor and Stator Slot Geometries of 16 Pole Motor	46

Table 18. Variable and Limits for Optometric Study of 16 Pole Motor.....	46
Table 19. Optometric Study Calculations for 16 Pole Motor.	46
Table 20. Results of Optimization for Rotor and Stator Geometry - 16 Pole.....	47
Table 21. Results of Optimization for Rotor and Stator Slot Geometry - 16 Pole	48
Table 22. Rated Performance Characteristics for 2 Pole vs. Optimized 16 Pole Motor.....	48
Table 23. Values for Rotor and Stator Geometries of 8 Pole (Original) Motor	53
Table 24. Values for Rotor and Stator Slot Geometries of 8 Pole (Original) Motor	54
Table 25. Values for Rotor and Stator Geometries of 8 Pole Motor	55
Table 26. Values for Rotor and Stator Slot Geometries of 8 Pole Motor	55
Table 27. Variable and Limits for Optometric Study of 8 Pole Motor.....	56
Table 28. Optometric Study Calculations for 8 Pole Motor.	56
Table 29. Results of Optimization for Rotor and Stator Geometry - 8 Pole.....	57
Table 30. Results of Optimization for Rotor and Stator Slot Geometry - 8 Pole	57
Table 31. Rated Performance Characteristics for 2 Pole vs. Optimized 8 Pole Motor.....	58

LIST OF FIGURES

Figure 1. B-H loop Comparing Vitroperm to a Ferrite Material	7
Figure 2. Solid Core Set (Left) and Cut Core Set (Right)	10
Figure 3. Flux Crowding in Adjacent Laminations	11
Figure 4. Experimental Configuration of Medium Solid Core	12
Figure 5. Core Loss for $f=20$ kHz	13
Figure 6. Core Loss for $f=50$ kHz	13
Figure 7. Core Loss for $f=100$ kHz	14
Figure 8. Core Loss for Fixed Induction Level of $B=1$ T	14
Figure 9. Toroid Wrapped With Wire	17
Figure 10. Progression from 3D Model to 2D Model	17
Figure 11. Progression from 3D Model to a 2D Model	18
Figure 12. Study of the Turn Spacing and Magnetic Field Distribution [26]	19
Figure 13. Effects of Air Gap	20
Figure 14. B-H Curve for HTX-012B	22
Figure 15. Material Input Screen for Core Loss vs. Frequency	23
Figure 16. Small Core Geometry Solid (Left) and Cut (Right)	25
Figure 17. Medium Core Geometry Solid (Left) and Cut (Right)	25

Figure 18. Various Conductor Types in ANSYS Maxwell	26
Figure 19. Core Loss Curves for Small Solid Core	29
Figure 20. Power Loss vs. Frequency Curve Fits -- Medium Solid Core.....	30
Figure 21. Power Loss vs. Current Curve Fits -- Medium Solid Core	30
Figure 22. Magnetic Concentration for Small Solid Core	31
Figure 23. Magnetic Concentration for Medium Solid Core	31
Figure 24. Equivalent Circuit for an AC Induction Motor	36
Figure 25. Typical Full Load Power Factors of Fixed Speed AC Motors [36]	38
Figure 26. AC Induction Motor Cross Section for a 2 Pole versus a 4 Pole Design [36]	39
Figure 27. Core Loss vs. Frequency for M600-50A.....	41
Figure 28. Material Data Input Screen for Core Loss vs. Frequency	42
Figure 29. 24 Pole (Original) Induction Motor.....	43
Figure 30. Rotor and Stator Geometry Variables	44
Figure 31. Torque vs. Speed Curve for 2 Pole Motor.....	49
Figure 32. Torque vs. Speed Curve for Optimized 16 Pole Motor.....	49
Figure 33. Flux Lines for 2 Pole Motor	51
Figure 34. Flux Lines for Optimized 16 Pole Motor	51
Figure 35. Magnetic Field Strength for 2 Pole Motor	52
Figure 36. Magnetic Field Strength for Optimized 16 Pole Motor.....	52
Figure 37. 8 Pole (Original) Motor	53
Figure 38. Rotor and Stator Geometry Variables	54
Figure 39. Torque vs. Speed Curve for 2 Pole Motor.....	58
Figure 40. Torque vs. Speed Curve for Optimized 8 Pole Motor.....	59

Figure 41. Flux Lines for 2 Pole Motor	60
Figure 42. Flux Lines for Optimized 8 Pole Motor	60
Figure 43. Magnetic Field Strength for 2 Pole Motor	61
Figure 44. Magnetic Field Strength for Optimized 8 Pole Motor.....	61

ACKNOWLEDGMENTS

I would like first thank my parents for all the financial, emotional, and spiritual support they have given me throughout my life. Even after years and years of engineering studies, I still can't figure out how they do it. Second, I would like to thank Brandon Grainger and Dr. Tom McDermott as the two largest contributors to helping me finish this thesis. Without their direction, I would not have completed this project.

I would like to thank Dr. Gregory Reed for funding me as a graduate student and for providing me with the opportunity to work on the ARPA-e grant. Working under you has been an eye opening experience. You have provided me with a fantastic working environment, at a top university, with a tremendous research team. Through your guidance, I was directed down a path of study that I would have never considered. Your influence has undoubtedly shaped my future into something more than it ever could have been.

I would like to thank Dr. Mao for all the help and guidance that you have brought to the research group. Your love of knowledge and passion for education has been an inspiration throughout my time as a graduate student.

I would like to thank the members of the research team and my friends: Hashim Al-Hassan, Adam Sparacino, Emmanuel Taylor, Ansel Barchowski, Raghav Khanna, Matthew Korytowski, Partick Lewis, and Alvaro Cardoza. In this group I would also like to thank my

editor at Winking Owl Writing. You all have put up with my antics and distractions for a long time, and I thank you for not becoming too upset with me.

Finally, I would like to thank my girlfriend Abigail Adkins and my close friend Steve Denninger for all their moral support throughout my graduate studies. Without your patience, understanding, and love, I would have seriously struggled to complete my work.

1.0 INTRODUCTION

Recent DOE reports convey the need for the advancement of soft magnetic materials for applications in high frequency, medium voltage, MW scale power electronics and grid integration technology [1]. Increases in DC power conversion and DC loads also motivates research into new topologies containing high-frequency DC-to-DC power converters, 0. The soft magnetics used in these power electronics can occupy significant space, require extensive cooling, and limit designs, 0. Operation at higher frequencies allows for reductions in converter size and weight 0,0, but conventional magnetic materials used in power converters rely on large grain sizes and significant concentrations of non-magnetic species, a combination that enables them to operate optimally at either high inductions or high frequency. Current commercial magnetic core materials are limited by low saturation inductions, in the case of ferrites, or they are limited to low frequency applications because of unacceptable losses at high frequencies, in the case of Si-Steels. Nanocomposites combine the soft magnetic strengths of amorphous core materials with the more attractive saturation inductions of crystalline metals a combination naturally well suited for high frequency converter applications 0,0.

The operation of power converters at higher frequencies is limited by increased losses in this regime, a trend accounted for by the Steinmetz Equation, (1.1), which relates the operating frequency, f , and saturation induction, B , to power loss.

$$P_L = 2f^\alpha B^\beta \quad (1.1)$$

In this equation the material dependent, empirically determined Steinmetz Coefficients, $\alpha(\sim 2)$ and $\beta(\sim 1-2)$, account for all core losses, in which hysteretic, anomalous, and conventional eddy currents losses are predominant. Noncore winding losses and switching losses in the semiconductor components compound these core losses. The operating frequency of a transformer is determined by optimizing the size reductions while taking into account the increase in losses at higher frequencies.

An exhaustive development of nanocomposites, such as FINEMET, NANOPERM, and HITPERM, has shifted the focus of research towards optimizing these materials' properties specifically for their use in state of the art power converters, [12]. Combinations of compositional additions and novel processing techniques have produced nanocomposites with permeability, $\mu > 10^5$, saturation induction, $B_s > 1.6\text{T}$, resistivity, $\rho > 150\mu\Omega\text{-cm}$, thickness, $t < 15\mu\text{m}$, temperature stability up to 300°C , and overall core losses less than 20W/kg at 10kHzT , a unit convention set by the Advanced Research Project Agency – Energy (ARPA-E).

This research first examines the prediction of Steinmetz coefficients of nanocomposite based magnetic materials using ANSYS to simulate high frequency operation. Then, an investigation is made into the scaling effects between bench top toroidal transformers of various sizes and geometries using simulation and experimental results. Finally, a study is conducted to observe the achievable size reduction for several induction motor designs that employ a novel nanocomposite material. This study also employs ANSYS software and models motors that are currently in operation.

2.0 BACKGROUND

2.1 PURSUIT OF HIGH SWITCHING FREQUENCIES

In 2012, the US alone had a net power generation of 4,054,485 thousand megawatthours. Generated power must be transformed by power electronics or conditioning systems to establish compatibility with transmission and distribution systems. In their Power Electronics Research and Development Program Plan from 2011, the D.O.E stated that, “Approximately 30% of all electric power currently generated uses PE somewhere between the point of generation and distribution. By 2030, it is expected that 80% of all electric power will flow through PE” [8]. Therefore, increased efficiency over a large scale could result in substantial savings by reducing energy demand and significantly reducing emissions.

Advancements in active components allow for much higher switching frequencies to be achieved. This has both enabled smaller passive components to be used in these applications and allowed for better harmonic filtering [9],[10]. A successful design of the passive components minimizes the losses of the magnetic material and the windings. High-frequency losses are mainly comprised of anomalous eddy currents, and they generate heat through I^2R losses in the magnetic material. This heat must be dissipated to maintain the integrity of the material which poses a new challenge, given that passive components are scaled down and have less surface area over which to dissipate heat. Understanding these losses as they relate to both material

properties and the geometry of the components is a driving force behind the research described in this paper.

2.2 A BRIEF EXPLANATION OF HIGH-FREQUENCY SWITCHING, SIZE REDUCTION, AND MATERIAL PROPERTIES

2.2.1 Faraday's Law

Low loss inductive switching is made possible by soft magnetic materials. By using increased switching frequency, the inductive components employed can be reduced in size; this process is described in Faraday's equations. If we consider an ideal toroid of inductance (L), permeability (μ), number of turns (N), effective length (l), cross sectional area (A), driven by an AC current, then we have Equation (2.1):

$$V = -NA \frac{dB}{dt} = -L \frac{dI}{dt} = -LI_0 \omega \cos(\omega t) = -\frac{\mu * N^2 * A}{l} I_0 \omega \cos(\omega t) \quad (2.1)$$

This equation is applicable for a constant maximum voltage of (V) and an AC current of $I_0 \omega \cos(\omega t)$. We can see from Faraday's law of induction that area (A) is inversely proportional to the frequency ($\omega = 2\pi f$). Therefore, when we increase the switching frequency, we are able to reduce the size of our toroid. 0

2.2.2 Steinmetz Equations and Core Loss

The most commonly used equation for calculating core loss is the Steinmetz Equation (2.2) 0:

$$P_c = k * f^\alpha * B^\beta \quad (2.2)$$

This loss, (P_c) , is determined from a sinusoidal driving frequency and includes both hysteresis and eddy current losses from changes of magnetization at a frequency (f) . The windings around the toroid produce a field H that is then amplified by the core. When the windings are in a single layer and closely packed, the winding losses are described by Equation (2.3) 0.

$$P_w = I_{RMS}^2 R = .5 * \left(\frac{B * l}{(\mu * \varphi * N)} \right)^2 * \frac{\rho l}{A_c} \quad (2.3)$$

This equation takes l to be the length of the wire, N to be the number of turns, ρ to be the conductor resistivity, A_c to be the conductor cross section, and φ to be some geometric constant.

2.2.3 Winding Loss – Skin and Proximity Effects

The conductor cross section shrinks with increasing frequency due to skin effect which explains that as frequency increases, current begins to flow on the surface of a conductor 0. In high frequency applications, smaller toroid cores limit the space available for windings. In these cases, the single conductors often times lie closely packed and on top of each other so the core is treated as being wound with litz.

Proximity effect is the phenomena of current flowing in loops or forming concentrations due to the presence of magnetic fields generated by nearby conductors; this occurrence is characteristic of litz wire and affects winding losses 0.

2.2.4 Core Loss, Winding Loss, and Permeability

As long as the core of a toroid is not in saturation, we can assume the Steinmetz coefficients to be constant over a given frequency range. For this range, the core loss is linear on a log-log loss vs. frequency plot. Winding losses change their slope with increased frequency due to the aforementioned skin and proximity effects [10]. By lowering the permeability of the core material, the material stores more inductive energy per cycle but also requires higher current (or more turns) to reach a desired induction [10]. Therefore, there is a cross over point, for increasing the frequency, at which the winding losses will outweigh the additional stored inductive energy in the core.

2.3 ARPA-E MATERIAL – A NOVEL MATERIAL AND IMPLICATIONS

Currently, 60Hz utility-scale transformers are made up of Si-Fe electric steels while high frequency applications turn to ferrites. New developments in material processing, such as rapid solidification and controlled nanocrystallization, have led to new amorphous/nanocrystalline nanocomposite soft magnetic materials. Utility and grid transformers made with these new Fe-based amorphous materials can be operated with significantly higher efficiencies [12] [12].

Moreover, these nanocomposite magnetic materials can operate exceedingly well at high switching frequencies if manufactured properly; they have a unique nanostructure which grants them superb soft magnetic properties due to random exchange interactions between the grains, mediated by an amorphous matrix. The permeabilities of these nanocomposites can be optimized by magnetic field annealing. For a typical commercial nanocomposite (Vitroperm)

and a typical ferrite, the static B-H loops illustrate that Vitroperm has a lower coercivity (related to losses per cycle) and a higher saturation induction (see Figure 1) 0. This is very attractive for high frequency transformer applications [13],0.

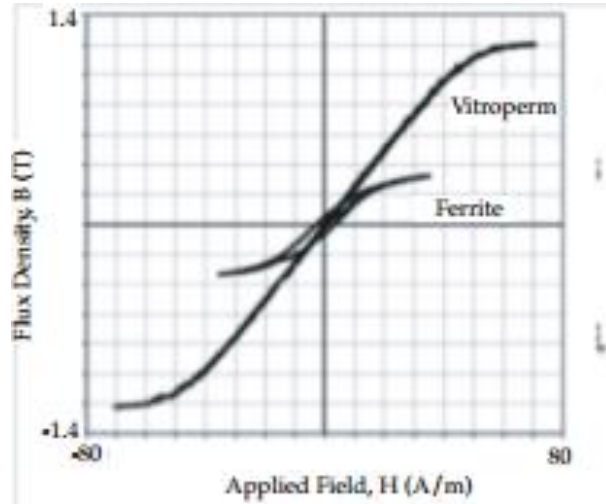


Figure 1. B-H loop Comparing Vitroperm to a Ferrite Material

The ARPA-e Solar ADEPT program team, including Carnegie Mellon University, SPANG Magnetics, and Los Alamos National Lab, has developed and are continuing to refine a set of nanocomposite materials that have considerable potential for excellent properties at high switching frequencies. The research presented in this thesis is focused on a HTX-012B, a nanocomposite developed by the ARPA-e project team, with low coercivity and low permeability.

2.4 PROCESS FOR VALIDATING AND UTILIZING ANSYS MAXWELL

These nanocomposites are being developed for high frequency applications, and there are many design challenges that will arise (and that have become apparent) while investigating these

new applications. In order to save time and money, it is important to have simulation capabilities that are proven to be valid. To this point, there are several goals of this research.

The first is to prove that ANSYS Maxwell 16 is a valid option for simulating the core loss and scaling effects of the novel nanocomposite material, HTX-012B. This is done by obtaining experimental core loss results for toroids of various sizes and geometries. These results are then used to obtain the Steinmetz coefficients for each core. The core loss versus frequency data for one of the cores is used to create a material datasheet within ANSYS Maxwell. The material data for this initial core is then applied to all the ANSYS Maxwell models that are generated for toroids of various sizes and geometries. In this way, the simulation can be proven to valid for scaling effects and changes in geometry.

Each simulated toroid then has a range of currents and frequencies applied to it in order to obtain simulated core loss results. These simulated results are used to obtain Steinmetz coefficients for each core. Finally, the Steinmetz coefficients obtained through simulation are compared to the experimentally obtained Steinmetz coefficients in order to verify that the simulation is producing the same results as the experiments.

3.0 CORE MODELING

3.1 EXPERIMENTAL TOROID DATA

3.1.1 Geometry

Six circular, tape wound cores made of HTX-012B were manufactured for this research, each with a stacking factor between .9 and .97. These cores were wound, annealed, impregnated, cut, and tested by the technicians at Spang & Company – Magnetics division. Two sets of cores were fabricated with different geometries. One set is made up of solid uniform cores, the other set has cuts made at the 12 o'clock and 6 o'clock locations see the right and left image of Figure 2 respectively for the sets of cores. Three different sized cores were made for each geometry. The outer diameter for each size is 1.25 inch (small), 2.81 inch (medium), and 6.25 inch (large). The core geometries are summarized in Table 1. Before cutting the cores, all of them were first annealed and then impregnated. The size of the cut in the cores is 0.002 inches and the ratio of the inner to the outer diameters is kept above 0.82 to reduce flux crowding (this ratio is an industry standard).



Figure 2. Solid Core Set (Left) and Cut Core Set (Right)

Table 1. Core Sizes and Geometries

Core #	Remarks	Dimensions	grams	Area,cm ²
1	Impregnated	1.25"x1.0"x1.0"	42.7	0.649
2	Impregnated, cut	1.25"x1.0"x1.0"	43.4	0.657
3	Impregnated	2.81"x2.25"x1.0"	214.3	1.444
4	Impregnated, cut	2.81"x2.25"x1.0"	215.0	1.449
5	Impregnated	6.25"x5.0"x1.0"	1016	3.079
6	Impregnated, cut	6.25"x5.0"x1.0"	1067	3.236

3.1.1.1 Flux crowding

Before moving forward, it should be noted that flux crowding and saturation affect performance in toroidal cores. Flux always takes the path of highest permeability i.e. the lowest magnetic reluctance. See Equation (3.1) for an explanation,

$$R = \frac{F}{\varphi} = \frac{1}{\mu * A} \quad (3.1)$$

where F is the magnetomotive force, φ is the flux, μ is the permeability of the material and A is the cross-sectional area of the material. This property of flux is easiest to view in transformers with laminations. Flux will flow along a lamination until it meets its mate and there is an air gap. At this point, the flux will flow to the adjacent lamination to bypass the air gap. At higher

currents, the lamination that the flux flows into to avoid the air gap will begin to saturate. This will cause the excitation current to become nonlinear and causes the permeability of the adjacent lamination to drop. At this point the flux will flow through the air gap 0.

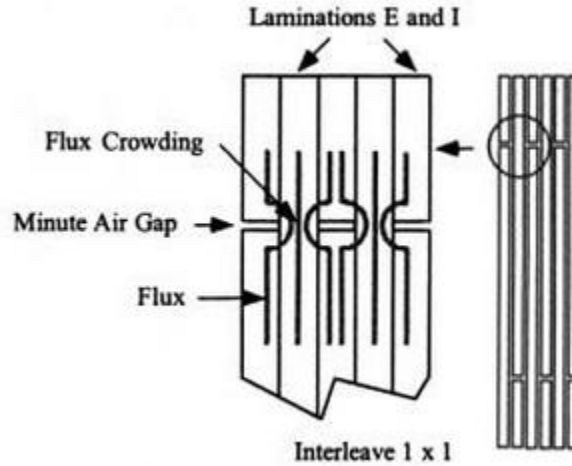


Figure 3. Flux Crowding in Adjacent Laminations

3.1.2 Experimental Core Loss Data

The core loss data was obtained for the six cores by first wrapping a primary and a secondary wire around the toroid and applying a range of excitations levels to the various core sizes at switching frequencies of 20 kHz, 50 kHz, and 100 kHz (see Table 2). Stranded 14 gauge AWG wire was used for both the primary and secondary side. The primary side was excited with a sinusoidal excitation and the core loss was recorded through the secondary side. Figure 4 displays how the medium sized solid core was wrapped. The small core geometry has one turn of wire while the medium and large has three turns. The RMS value of the core loss in W/kg was recorded for each combination of frequency and Tesla level (to evaluate the solid and cut cores both before and after impregnation). These results are also displayed in Table 2. Figure 5 through Figure 8 provides graphical representation of core loss.

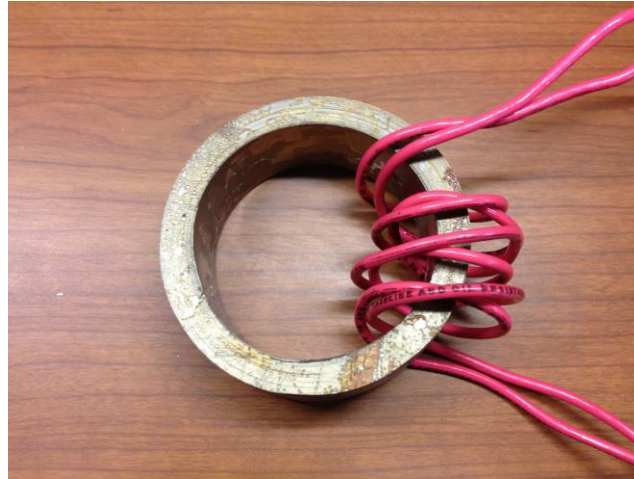


Figure 4. Experimental Configuration of Medium Solid Core

Table 2. Core Loss for Annealed, Impregnated, and Impregnated and Cut Cores

Core #	Dimensions	Remarks	Watt loss at 20 kHz, W/kg			Watt loss at 50 kHz, W/kg			Watt loss at 100 kHz, W/kg		
			0.1 T	0.2 T	0.5 T	0.05 T	0.1 T	0.2 T	0.025 T	0.05 T	0.1 T
1	1.25"x1.0"x1.0"	Annealed	0.8	3.2	18.2	0.9	3.7	14.0	0.8	3.1	11.7
2	1.25"x1.0"x1.0"		0.8	3.2	17.7	1.0	3.7	13.9	0.8	3.1	11.8
3	2.81"x2.25"x1.0"		0.8	3.0	17.5	0.9	3.5	13.3	0.7	2.9	11.2
4	2.81"x2.25"x1.0"		0.8	3.1	18.4	0.9	3.6	13.7	0.8	3.0	11.5
5	6.25"x5.0"x1.0"		0.8	3.1	18.8	0.9	3.5	13.6	0.7	2.9	11.2
6	6.25"x5.0"x1.0"		0.7	3.0	17.9	0.9	3.4	13.2	0.7	2.8	11.0

Core #	Dimensions	Remarks	Watt loss at 20 kHz, W/kg			Watt loss at 50 kHz, W/kg			Watt loss at 100 kHz, W/kg		
			0.1 T	0.2 T	0.5 T	0.05 T	0.1 T	0.2 T	0.025 T	0.05 T	0.1 T
1	1.25"x1.0"x1.0"	Impregnated	1.5	5.6	37.3	1.4	5.7	23.0	1.1	4.5	17.7
2	1.25"x1.0"x1.0"	Impregnated, cut	1.2	4.6	25.1	1.5	5.9	22.2	1.1	4.6	17.8
3	2.81"x2.25"x1.0"	Impregnated	1.5	6.2	37.9	1.4	5.5	21.9	1.1	4.2	16.9
4	2.81"x2.25"x1.0"	Impregnated, cut	1.6	6.5	34.1	1.6	6.2	24.3	1.2	4.8	19.0
5	6.25"x5.0"x1.0"	Impregnated	0.9	3.5	21.3	0.9	3.7	14.4	0.8	3.1	12.0
6	6.25"x5.0"x1.0"	Impregnated, cut	1.0	3.9	23.1	1.0	4.2	16.2	0.8	3.4	13.2

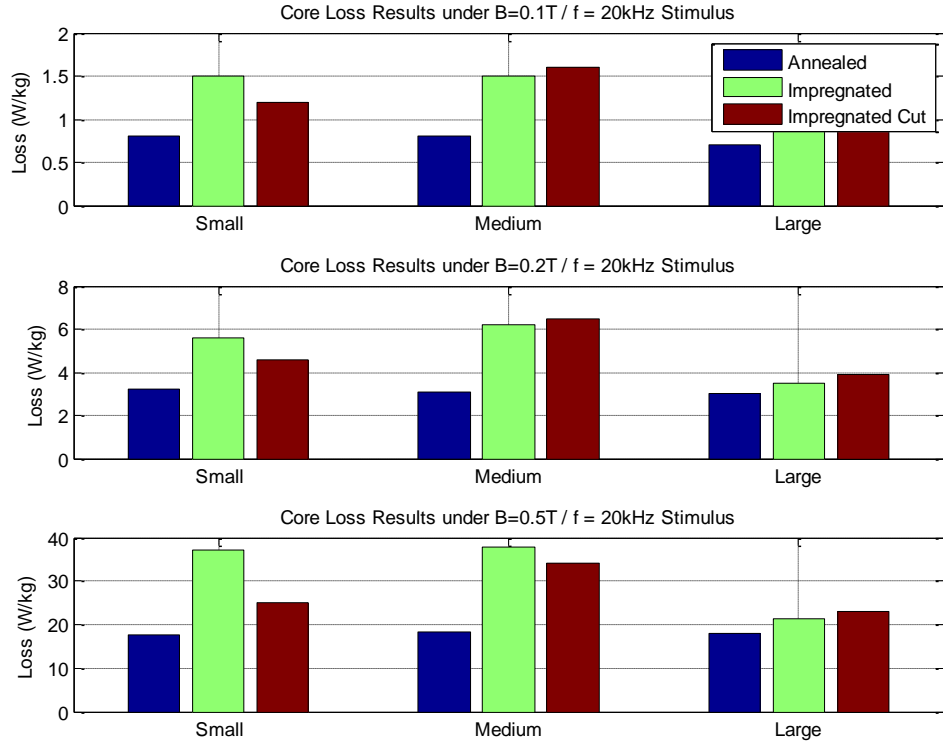


Figure 5. Core Loss for $f=20\text{ kHz}$

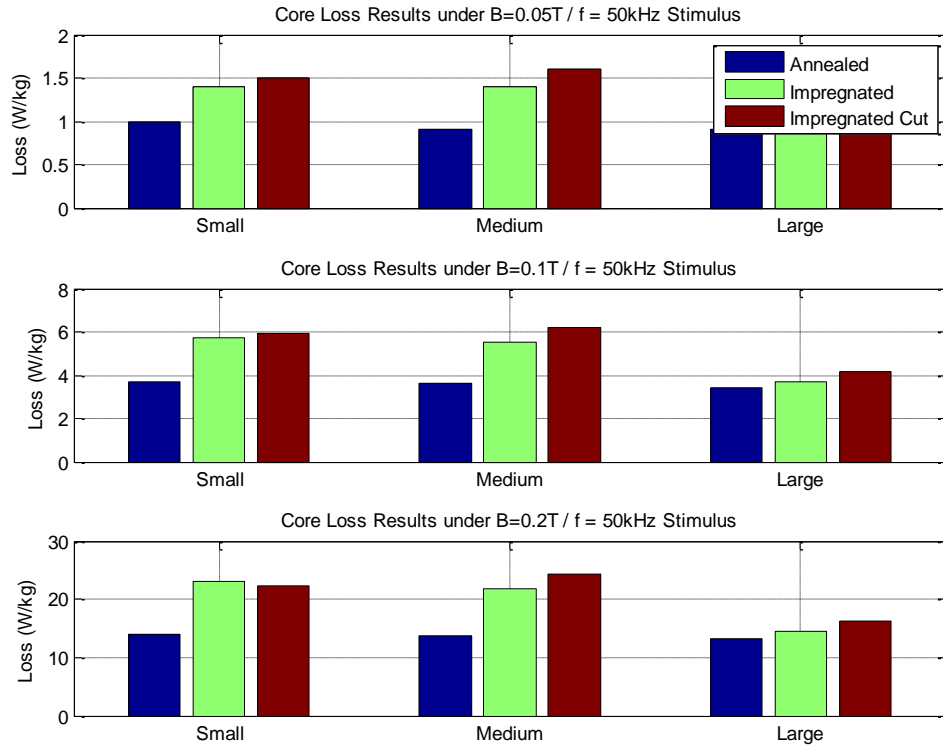


Figure 6. Core Loss for $f=50\text{ kHz}$

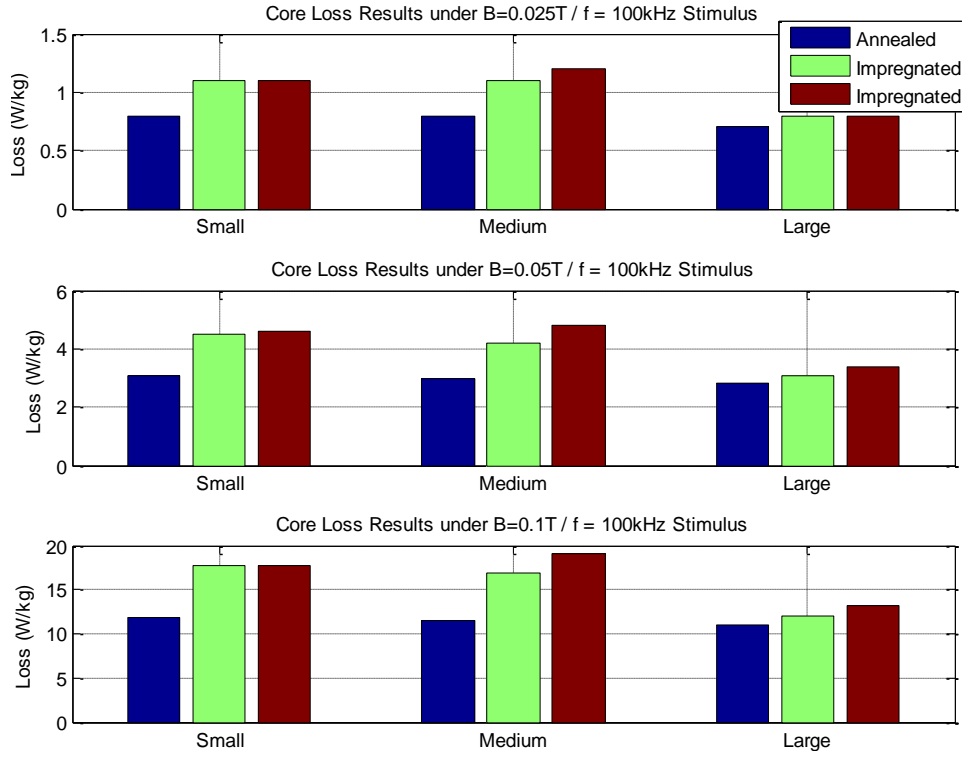


Figure 7. Core Loss for $f=100\text{ kHz}$

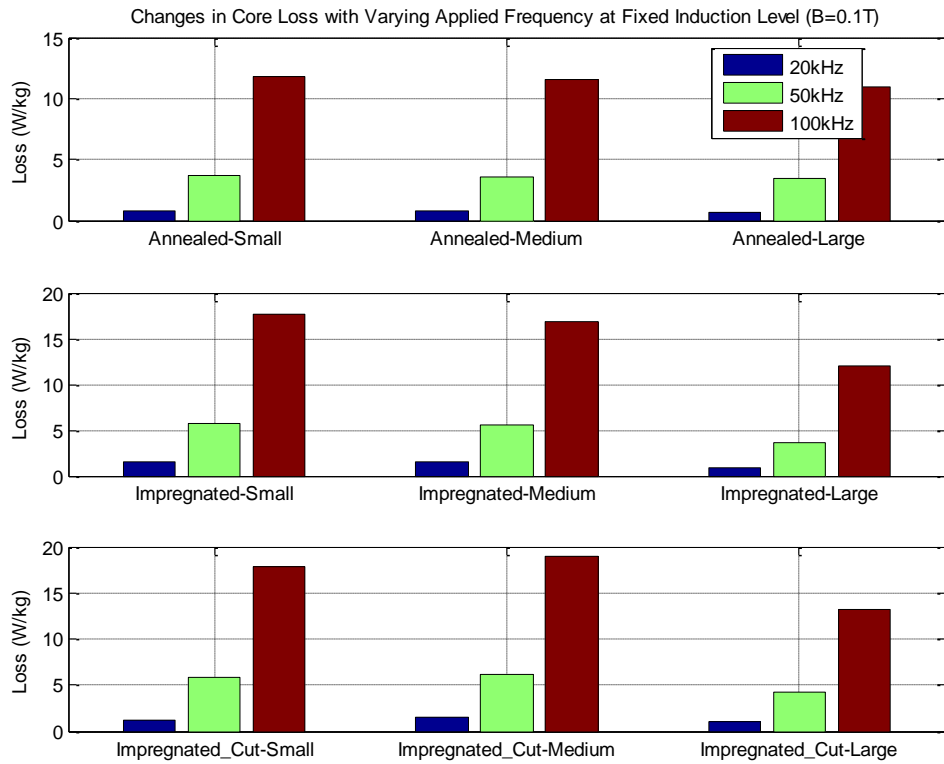


Figure 8. Core Loss for Fixed Induction Level of $B=1\text{ T}$

The figures depicting the experimental core loss data display several trends. Increasing the Tesla and frequency levels also increases core loss, which follows the Steinmetz Equation (1.1). The manufacturing step of impregnation increases the core loss/kg for each size. This, however, is an essential step as it ensures that the cores do not fall apart. Additionally, there is increasing loss from annealed, to impregnated, to impregnated and cut. Each step sacrifices core loss and lower permeability as displayed in Table 3.

Table 3. Permeability of Annealed, Impregnated, and Impregnated and Cut Cores

Core #	Dimensions	Remarks	Initial	Core #	Remarks	Initial
			permeability			permeability
1	1.25"x1.0"x1.0"	Annealed	64,544	1	Impregnated	21,169
2	1.25"x1.0"x1.0"		69,846	2	Impregnated, cut	2,843
3	2.81"x2.25"x1.0"		70,507	3	Impregnated	21,109
4	2.81"x2.25"x1.0"		68,118	4	Impregnated, cut	3,458
5	6.25"x5.0"x1.0"		69,407	5	Impregnated	45,356
6	6.25"x5.0"x1.0"		77,567	6	Impregnated, cut	12,398

Finally, core loss in W/kg for the large core is always the lowest. There are a number of explanations for this: the larger size could lead to better heat dissipation; there may be better coupling between (less air spacing between) the wire and the core; and the larger radius could lead to less core stress, among a number of other possible explanations. What is important to take away from all this data is the experimental Steinmetz coefficients obtained for each core, listed in Table 4.

Table 4. Steinmetz Coefficients for Experimental Cores

Core #	Dimensions	Remarks	Steinmetz coefficients		
			k	α	β
1	1.25"x1.0"x1.0"	Impregnated	1.4684	1.5467	2.0281
2	1.25"x1.0"x1.0"	Impregnated, cut	0.5927	1.6945	1.8964
3	2.81"x2.25"x1.0"	Impregnated	1.9061	1.4548	1.9877
4	2.81"x2.25"x1.0"	Impregnated, cut	1.2957	1.5314	1.9004
5	6.25"x5.0"x1.0"	Impregnated	0.6904	1.5967	1.9689
6	6.25"x5.0"x1.0"	Impregnated, cut	0.7305	1.6059	1.9630

Let us quickly recall Equation (1.1) here.

$$P_c = k * f^\alpha * B^\beta \quad (1.1)$$

The variables from Table 4 are substituted directly into the equation above to achieve core loss for each of the cores. By comparing the experimentally obtained coefficients to the coefficients obtained from the simulation, we are able to validate the models accuracy.

3.2 METHODS OF ANSYS MODELING

3.2.1 Introduction

To test core loss in a toroid, the core is wrapped with wire conductor in a helical design. This is similar to the toroid depicted in Figure 9. In order to expedite the simulation, a 2D cross section is taken of the 3D models. This progression is depicted in Figure 10. When a 2D model is created, the software is designed to assume that the model extends into the page a specific depth. The user sets this depth in the options and thus the third dimension is accounted for in the

software's analysis. Using a 2D model, allows for a less complex mesh and thus, faster run times.

There are two main methods of modeling conductors within ANSYS Maxwell 16. The first is the grouped conductor method, which allows for a faster simulation run time, but sacrifices accuracy in some situations. The second is the individual conductor method, which has a longer simulation run time, but is more accurate than the former. Both methods will be discussed in this section.

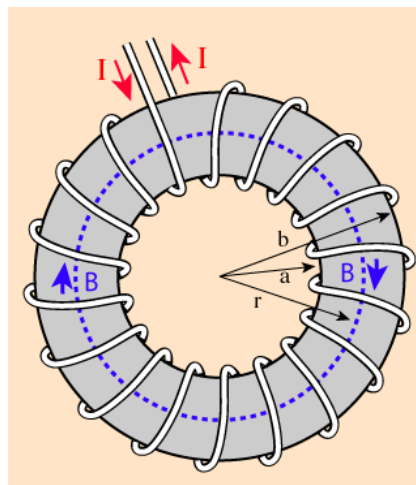


Figure 9. Toroid Wrapped With Wire



Figure 10. Progression from 3D Model to 2D Model

3.2.2 Modeling with Grouped Conductors

A helical design is a complicated geometry not only to model in many programs, but it is also computationally intensive to mesh. For this reason, the grouped conductor method models the cross section of 3D helix as a curved rectangle instead of a series of circles bred by a 2D cross section of a helix. The progression seen in Figure 11 depicts how a 3D winding geometry is transformed into a 2D rectangular layer 0.

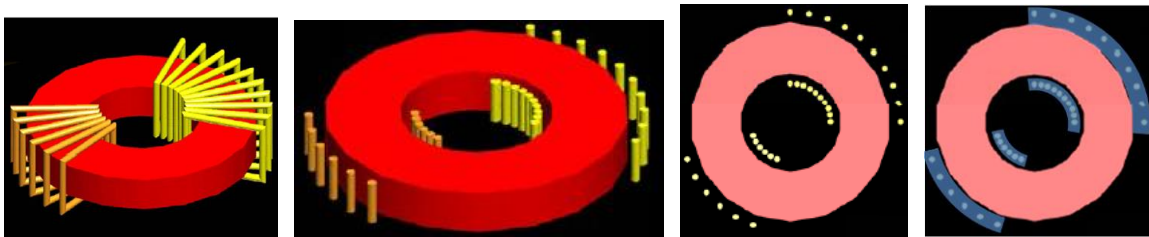


Figure 11. Progression from 3D Model to a 2D Model

Each rectangular layer can only be composed of one winding (i.e. as a primary set of windings versus a secondary set of windings, not individual conductors). With this method of modeling, large distances between conductors in the winding add to the error to the simulation. However, error can be kept to less than 10% if the winding fill factor is high 0.

3.2.2.1 The need for high form factor

To demonstrate this need for a high form factor, a team at ANSYS performed tests where the short circuit resistance and inductance were calculated using simulated round wires and then rectangles to replace them. This was performed for a frequency range from 100Hz to 1MHz. Figure 12 and Table 5 depict the results, showing that while the conductors are spaced closer together (with a high form factor), there is less error; and as the conductors move farther apart, the error increases 0.

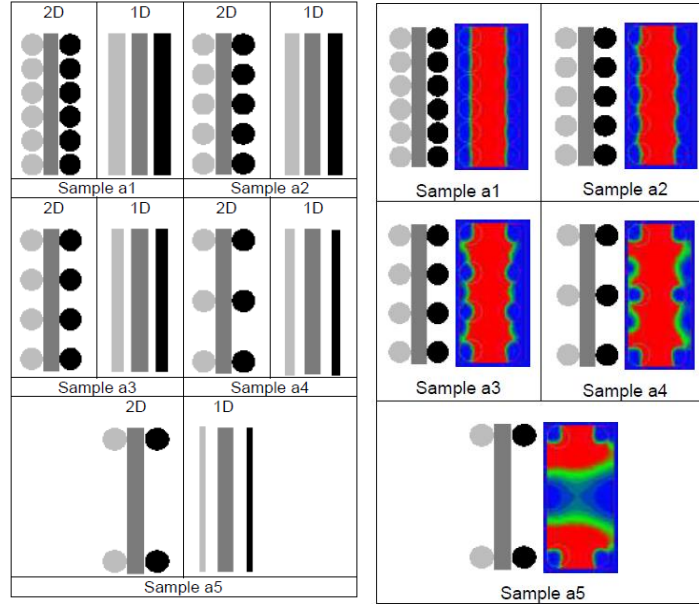
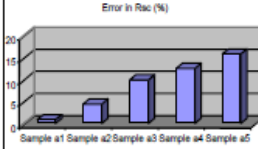
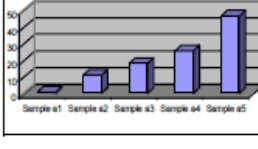


Figure 12. Study of the Turn Spacing and Magnetic Field Distribution 0

Table 5. Study of Spacing among Layers and Quantification of Errors at 100 kHz 0

	Short Circuit Resistance (mΩ)		
	1D	2D	Diff (%)
Sample a1	30.6	30.3	0.9
Sample a2	23.0	22.0	4.5
Sample a3	16.5	15.0	10.0
Sample a4	10.7	9.5	12.6
Sample a5	5.8	6.9	15.9
	Short Circuit Inductance (nH)		
	1D	2D	Diff (%)
Sample a1	285	287	0.7
Sample a2	201	227	11
Sample a3	131	160	18
Sample a4	76	102	25.5
Sample a5	35.6	66.6	46.5

3.2.2.2 Air Gap Considerations

Air gap is another concern when modeling individual wires as solid rectangular units given that “the fringing flux close to the air gap produces additional ‘proximity’ losses in the nearest conductors and should be accounted for” 0. Figure 13 depicts the typical magnetic fields

associated at the gap in a core's geometry. This air gap produces a large error when the open circuit transformer test is run, but very little error during the short circuit test. This is because in the open circuit test, most of the energy is stored in the fringing flux, while in the short circuit test, most of the energy is stored in the core Φ .

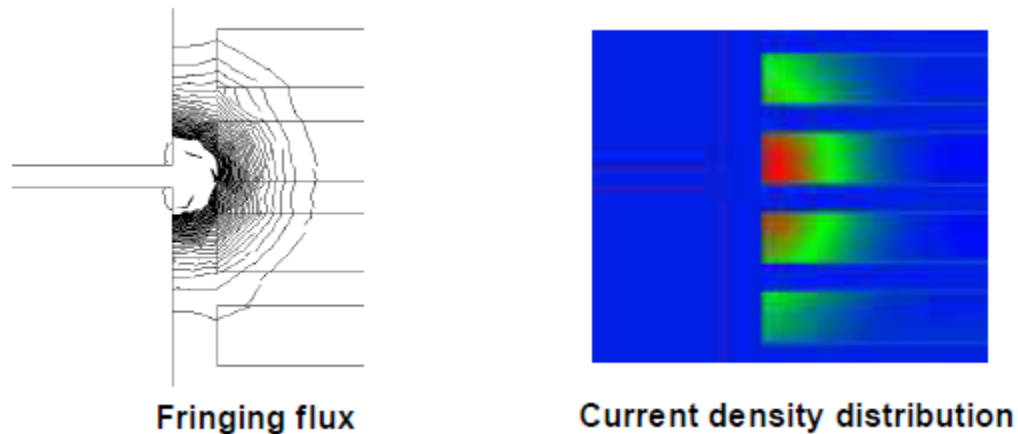


Figure 13. Effects of Air Gap

As stated previously, the grouped conductor method is valuable in certain situations, but not when the conductor stacking factor is low and/or when there is an air gap in the core geometry.

3.2.3 Modeling with Individual Conductors

Modeling with individual conductors simply leaves each conductor as a circle for a 2D model. This format can significantly increase simulation time and should be avoided for models that have many conductors and that fall within the safe geometries described in the previous section. The run time increases because each conductor must be individually meshed and analyzed during the simulation.

3.3 ANSYS MODELING OF THE CORE

3.3.1 Introduction

The objective of designing these models is threefold: to show that the software, ANSYS Maxwell 16, can produce the same results as the experiments for one size and geometry; to demonstrate that it is able to reproduce the experimental results for scaling the cores up and down; and to demonstrate that it can reproduce the same experimental results for changing geometries from solid to cut. This is to be done using the same material data.

In order to achieve these objectives, a model was created to simulate the medium sized solid core. The core loss versus frequency data was entered from the experimental test. The medium core experimental material data was then used for a small and large solid core, as well as a small, medium, and large cut core. The simulation results were then compared to the experimental results to verify the accuracy of the simulation.

3.3.2 Imputing Material Data

Before building the geometry, the material data was entered into Maxwell 16. A B-H curve was selected for the relative permeability. Experimental data was obtained from Spang Magnetics for the medium solid core. The experimental data and B-H curve can be seen in the Maxwell material data entry table which is displayed in Figure 14. The bulk conductivity was set to 500000 siemens/m, the mass density was set to 7800 kg/m³, and the core loss type was set to electric steel.

As an electric steel, the core loss coefficients needed to be calculated for the material properties. This was done by imputing the core loss versus frequency data that had been obtained through the experimental tests for the medium sized solid core. The data entered is displayed in Table 6 and shown in Figure 15.

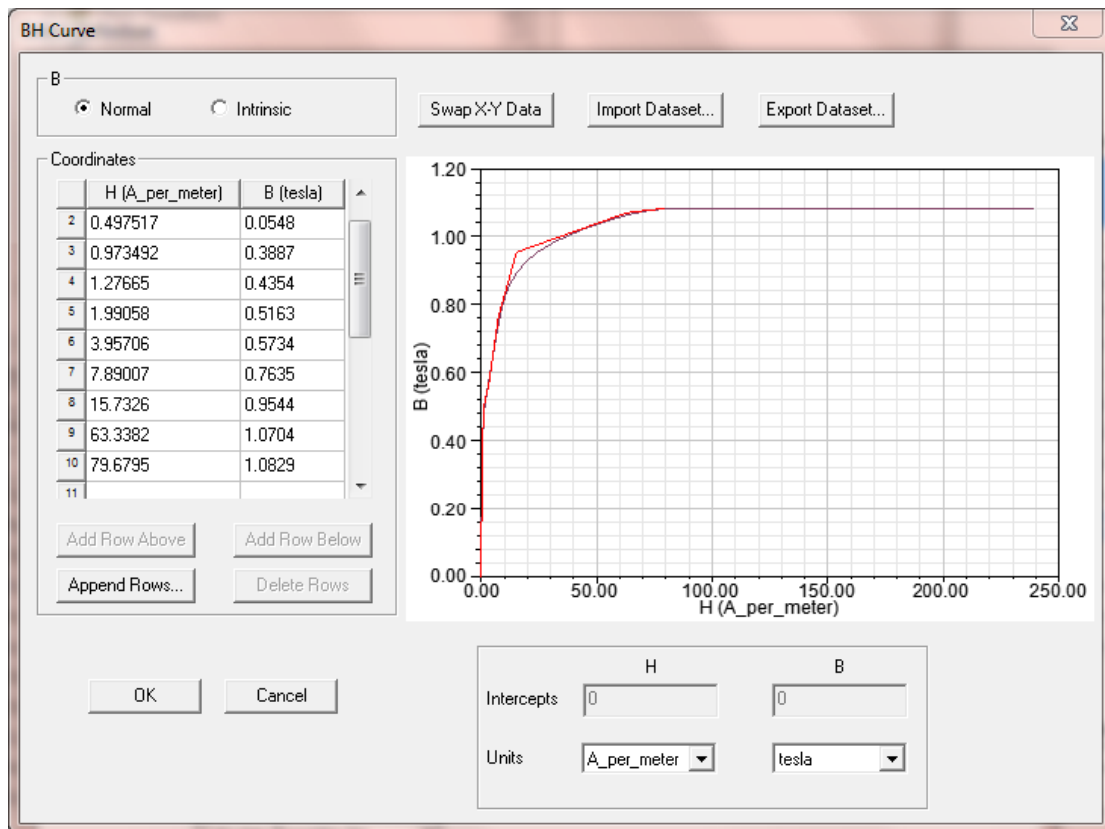


Figure 14. B-H Curve for HTX-012B

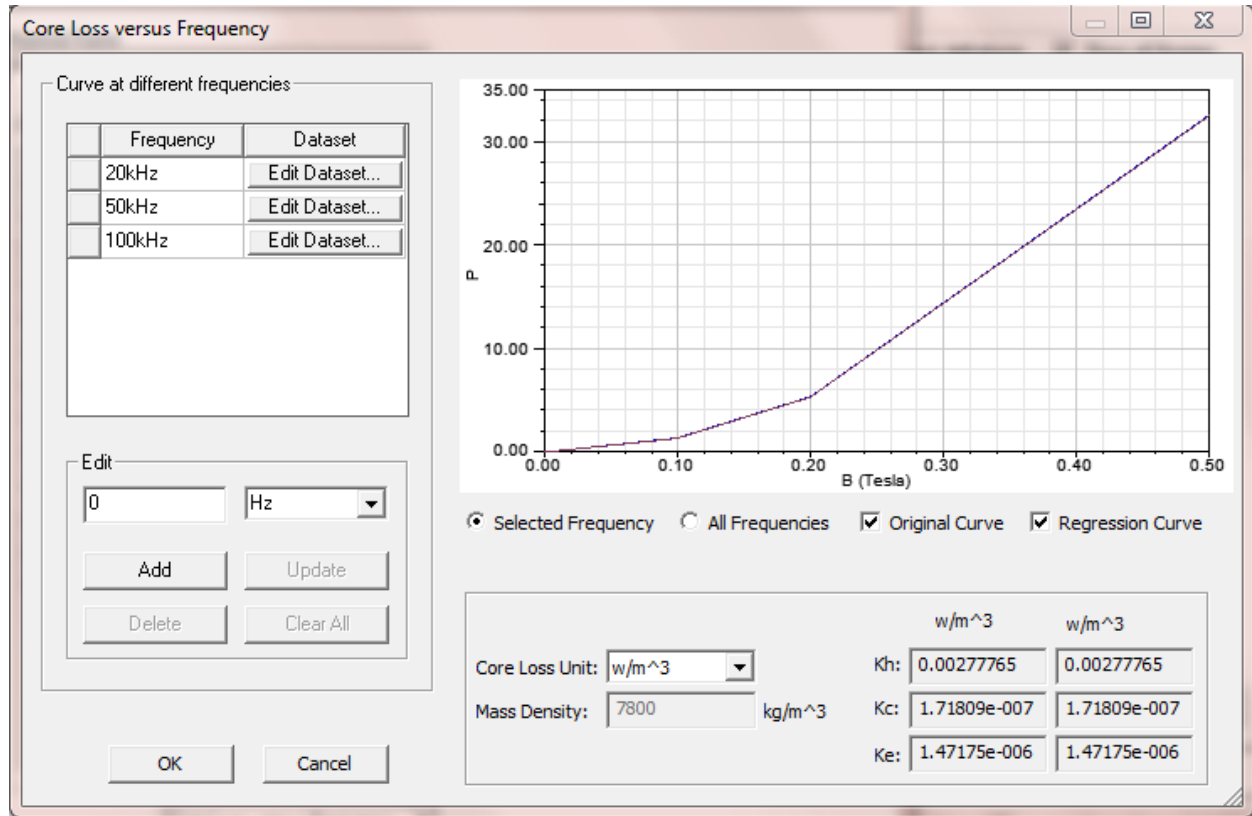


Figure 15. Material Input Screen for Core Loss vs. Frequency

Table 6. Loss vs. Frequency Data for Solid Medium Core – 20 kHz to 100 kHz

Core #	Watt loss at 20 kHz, W/kg			Watt loss at 50 kHz, W/kg			Watt loss at 100 kHz, W/kg		
	0.1 T	0.2 T	0.5 T	0.05 T	0.1 T	0.2 T	0.025 T	0.05 T	0.1 T
3	1.5	6.2	37.9	1.4	5.5	21.9	1.1	4.2	16.9

Under sinusoidal flux conditions, the core loss is computed using the following equation:

$$P_v = P_h + P_c + P_e = K_h f (B_m)^2 + K_c (f B_m)^2 + K_e (f B_m)^{1.5} \quad (3.2)$$

In this equation, B_m is the amplitude of the AC flux component, f is the frequency, K_h is the hysteresis core loss coefficient, K_c is the eddy-current loss coefficient, and K_e is the excess core loss coefficient [24]. Based on the results in Table 6 and those produced by Equation (3.2), the

coefficients in Table 7 were obtained. Figure 15 also displays these coefficients in the bottom right.

Table 7. Core Loss Coefficients for Solid Medium Core

K_h	0.00277765
K_c	0.00000017
K_e	0.00000047

3.3.3 Building the Models

3.3.3.1 Introduction

The model geometry is made up of the core and the conductors. As a point of reference, Figure 4 displays the geometry that is being recreated. A 2D model of the experimental set up for the medium and large cores yields a solid core with six conductors on the inside and the outside of the core (three for the primary and three for the secondary). The small core only has one turn of conductors and thus yields two conductors on the inside and two on the outside of the core.

The individual conductor method was selected for a variety of reasons. A grouped conductor method would not have captured the effect of the secondary winding, given that the group conductor method can only represent one winding. The stacking factor was not significantly high, illustrated in Figure 4, which would lead to errors in the simulation results. Finally, the gaped cores had to be modeled with individual conductors to account for the fringing flux. By switching between the grouped versus individual conductor method, unknown errors could have been introduced into the results based on the different assumptions that each methods makes about the conditions of the model.

3.3.3.2 Geometry Models

The small and medium geometries are displayed in Figure 16 and Figure 17 respectively. The large core geometry is not displayed as it is a larger version of the medium geometry and looks the same. The material for the conductors was selected from the ANSYS material database and was listed as copper. The diameter of the conductors was set to .0641" which is the listed diameter for a 14 AWG gauge wire.

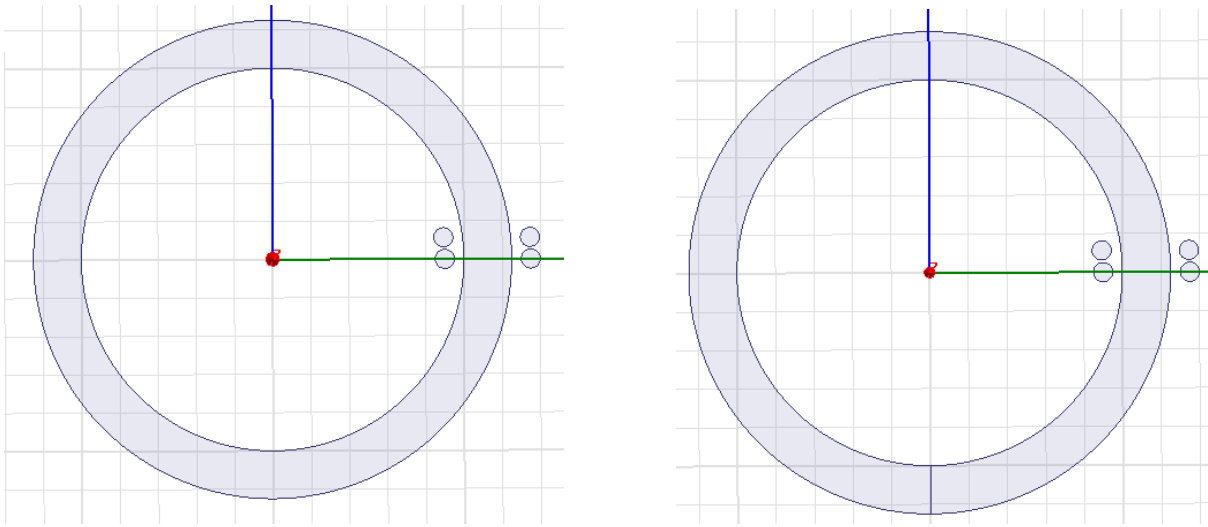


Figure 16. Small Core Geometry Solid (Left) and Cut (Right)

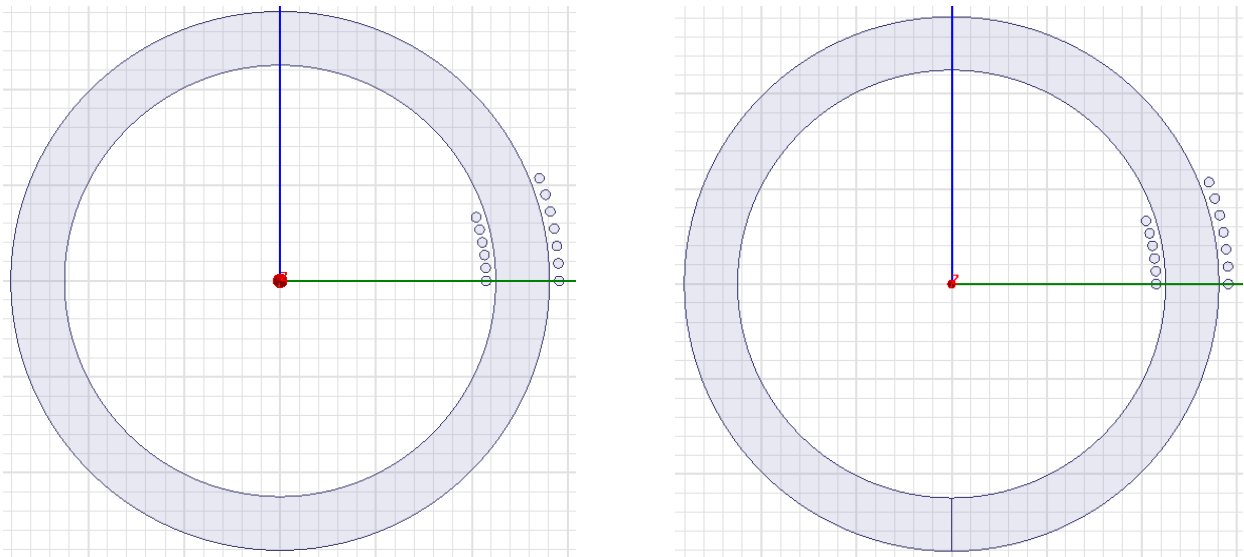


Figure 17. Medium Core Geometry Solid (Left) and Cut (Right)

3.3.3.3 Conductor Types

Within ANSYS Maxwell 16, there are three available conductor types: stranded, solid, and parallel. When a stranded conductor type is selected, Maxwell 16 does not calculate the losses due to eddy current or displacement currents. It also assumes a uniform distribution of current throughout the conductor. A solid conductor type includes eddy current and displacement current losses in the calculation and models skin effect. Finally, a parallel conductor type models parallel conductors and the eddy current and displacement current losses that come with that configuration. Figure 18 shows the differences between the three types of conductors available 0.

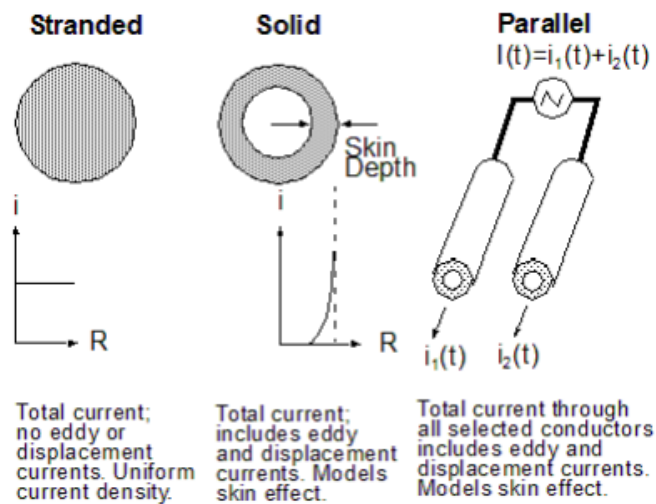


Figure 18. Various Conductor Types in ANSYS Maxwell

The stranded conductor model allows for faster simulation run time, because there are fewer calculations that the software must complete. For this reason, it is preferable to prove that winding losses can be considered negligible.

To examine whether skin effect must be accounted for, the skin depth must be greater than the radius of the interior strands of the conductor. The formula to calculate skin depth is given by Equation (3.3):

$$\delta = \sqrt{\frac{2\rho}{2\pi f \mu_R \mu_0}} \quad (3.3)$$

Here, ρ is the resistivity of copper (here $1.673 \mu\Omega - cm$), f is the frequency, μ_R is the relative permeability (here 1), and $\mu_0 = 4\pi * 10^{-7}$ Henries/meter. Table 8 displays the skin depth for the tested frequency levels. The 14 gauge AWG stranded wire is comprised of 19 gauge AWG strands with a radius measuring .01795". The table shows, this is below the skin depth levels for this frequency range. Thus we can say that the skin effect is negligible.

Table 8. Frequency and Skin Depth

Frequency	Skin Depth
20kHz	0.05398
50kHz	0.036245
100kHz	0.025629

To verify that these calculations were correct and that it was acceptable to use the stranded rather the solid conductor type, several iterations of the solid, medium core simulation were run with the solid conductor type and then compared to the stranded conductor type results. Core and winding losses were calculated for the solid conductor type and the Steinmetz coefficients were derived from these. The differences in the derived Steinmetz coefficients from each set were negligible, so the rest of the simulations were run with the stranded conductor type.

3.3.3.4 Applying Excitations

Excitations were applied to the inner and outer conductors, of the primary winding, and a parametric sweep of the frequency and current ranges were made. For the inner conductors, the current was directed out of the page while the outer conductors' current was directed into the page. The current and frequency levels are displayed in Table 9.

Table 9. Frequency and Current Range

Frequency (kHz)	Current (A)
20	0.0005
50	0.003
100	0.005
	0.01
	0.013
	0.03
	0.06

3.3.4 Understanding the Data and Results

To calculate Steinmetz coefficients, the core loss data for the parametric sweep is first exported from Maxwell 16 into Excel. Figure 19 depicts the core loss curves for a parametric sweep of the levels in Table 9 for the small solid core. Once the data is entered into Excel, the RMS value of the core loss is obtained for the steady state condition for each combination of core loss and frequency.

Table 10 lists the steady state, RMS core loss data values obtained for the small solid core for a portion of the combinations. To calculate α , a power curve fit is applied to the curve of core loss versus frequency while the current remains fixed. To calculate β , a power curve fit is applied to the curve of core loss versus current while the frequency remains fixed. See Figure

21 and Figure 20 respectively for curve fits determining α and β . The average of the coefficients is calculated and represents the simulated coefficient for each geometry. A table of the simulated and experimental coefficients for each core and the error between them is presented and discussed in section 3.4.

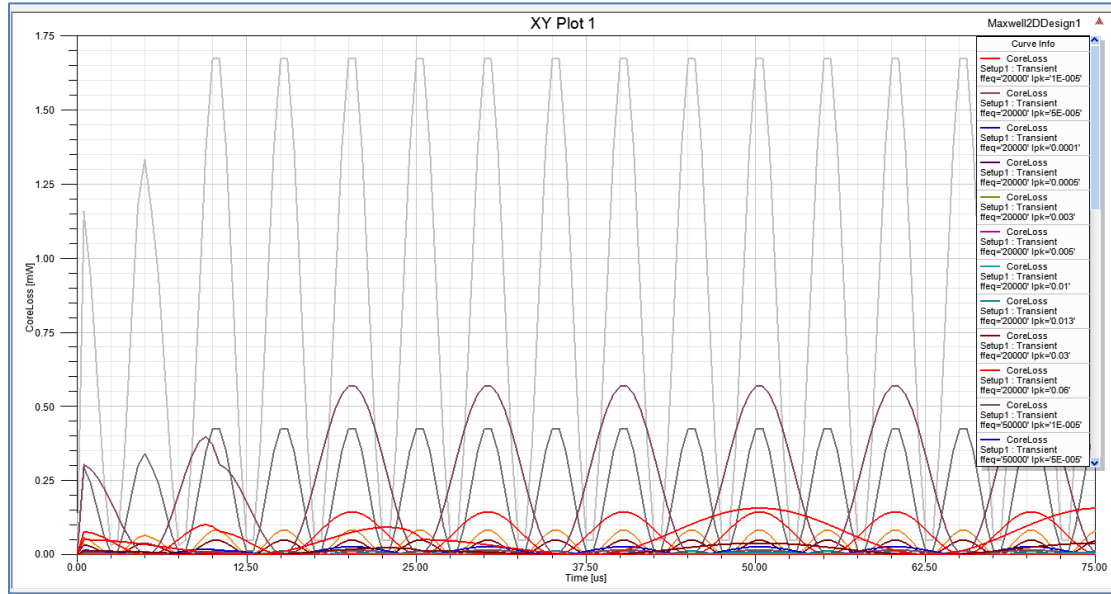


Figure 19. Core Loss Curves for Small Solid Core

Table 10. Core Loss (mW) for Small Solid Core

Frequency	Current (A)		Core Loss (mW)		
	0.005	0.01	0.013	0.03	0.06
20000	5.965E-04	2.264E-03	3.764E-03	1.926E-02	7.525E-02
50000	2.585E-03	9.832E-03	1.636E-02	8.382E-02	3.278E-01
100000	8.004E-03	3.057E-02	5.093E-02	2.618E-01	1.026E+00

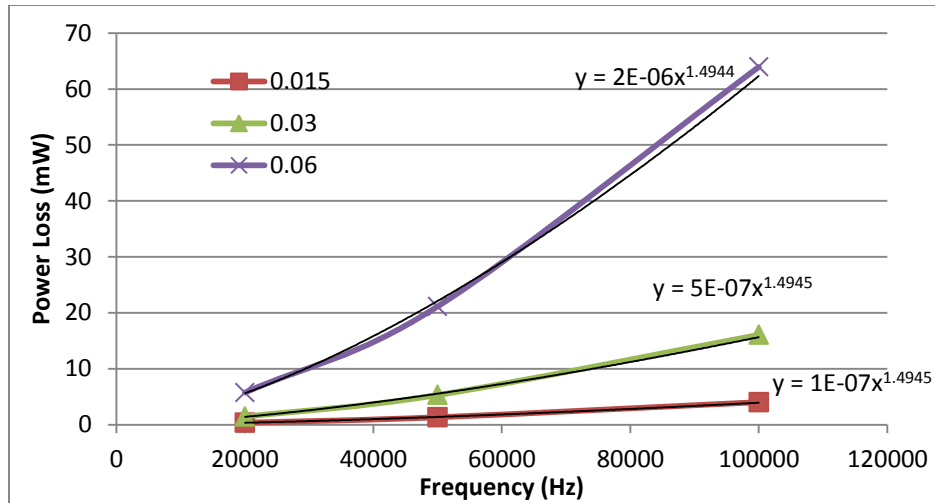


Figure 20. Power Loss vs. Frequency Curve Fits -- Medium Solid Core

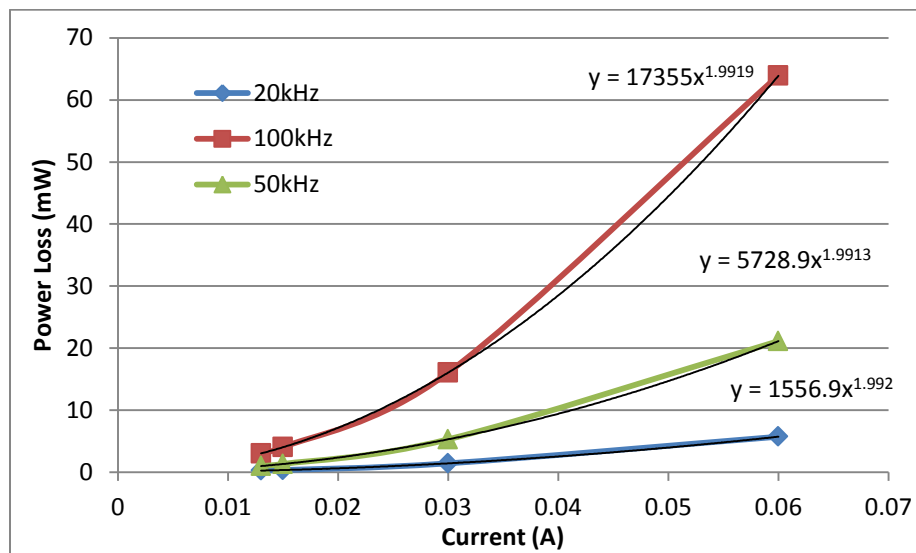


Figure 21. Power Loss vs. Current Curve Fits -- Medium Solid Core

Finally, the magnetic field plots are depicted to demonstrate that the core is operating as expected and is within the tested Tesla levels. Figure 22 and Figure 23 depict the small and medium solid cores, where the flux is concentrated around the center of both as expected. In addition, the maximum Tesla level is below the range tested experimentally. Figure 22 and Figure 23 highlight the small and medium cut core. In the same way, these cores are behaving as

expected and are not saturated. As before, the large core geometry is not depicted as it is essentially the same as the medium core geometry.

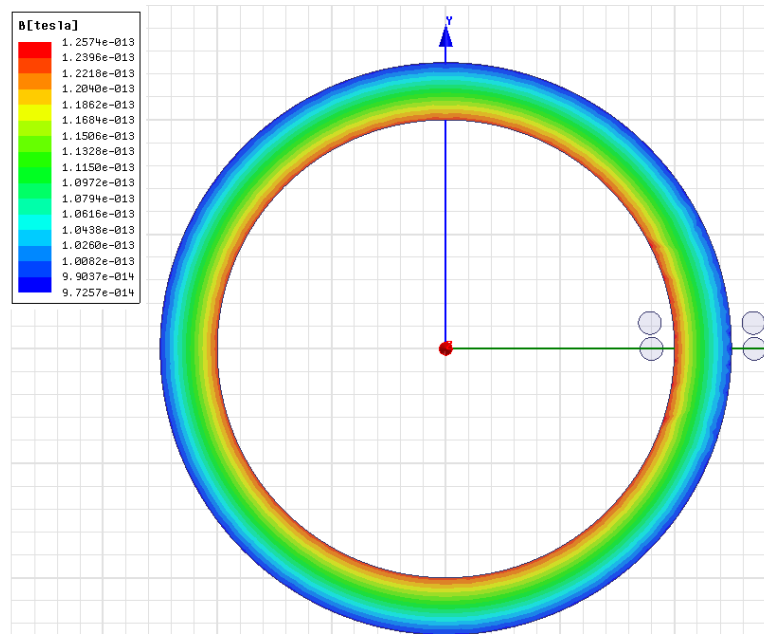


Figure 22. Magnetic Concentration for Small Solid Core

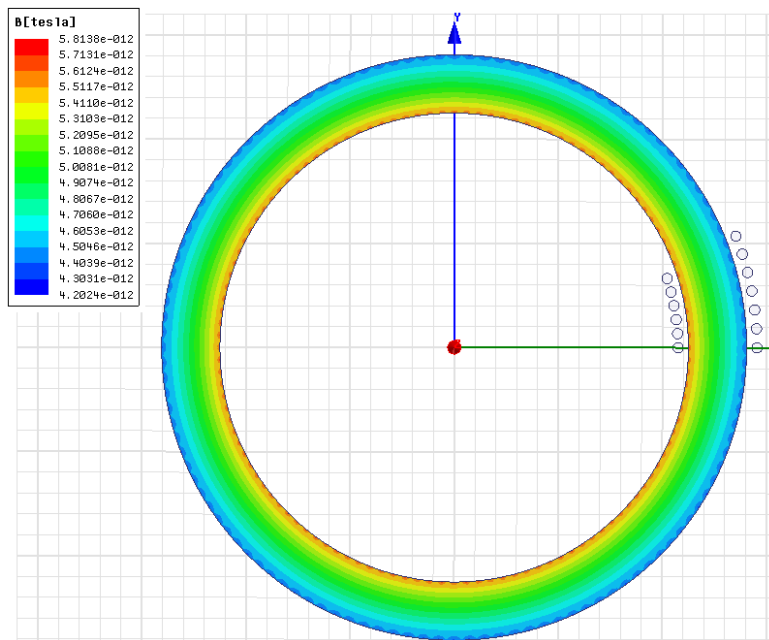


Figure 23. Magnetic Concentration for Medium Solid Core

3.4 COMPARING EXPERIMENTAL AND SIMULATED RESULTS

3.4.1 Analyzing the Results and Observing Error

Table 11 contains the experimental and simulated results as well as the error between them. The error for α and β is, by and large, under 3% except for the small impregnated cut core, which is 5%. There are many factors that can contribute to the error in these results. This list includes variable manufacturing tolerances, variable coupling (air space) between the windings and the core, differences in stress in each core due to differences in radii, and others. Based on all the factors listed, and after discussing with Spang Magnetics, an error of 5% constitutes ANSYS Maxwell's successful modeling of the experimental cores.

Table 11. Experimental and Simulated Results for α and β with Error

Core #	Dimensions	Remarks	Experimental Steinmetz Coefficients		Simulated Steinmetz Coefficients		α error	β error
			α	β	α	β		
1	1.25"x1.0"x1.0"	Impregnated	1.5467	2.0281	1.56	1.96	1%	3%
2	1.25"x1.0"x1.0"	Impregnated, cut	1.6945	1.8964	1.617	1.956	5%	3%
3	2.81"x2.25"x1.0"	Impregnated	1.4548	1.9877	1.494	1.992	3%	0%
4	2.81"x2.25"x1.0"	Impregnated, cut	1.5314	1.9004	1.563	1.968	2%	3%
5	6.25"x5.0"x1.0"	Impregnated	1.5967	1.9689	1.579	1.987	1%	1%
6	6.25"x5.0"x1.0"	Impregnated, cut	1.6059	1.9630	1.578	1.987	2%	1%

3.4.2 Conclusions

Observing the simulated data and flux plots from the ANSYS Maxwell 16 models produced experimental α and β coefficients for HTX-012B. With the low error, and a range of tested sizes and geometries, it can be safely assumed that ANSYS Maxwell 16 is accurate in determining both scaling effects and changes in geometry. In the next section, this software will be used to explore motor design.

4.0 MOTOR MODELING

4.1 INTRODUCTION

ARPA-E advances high-potential, high-impact energy technologies that are too early for private sector investment. With this in mind, the organization is very interested in moving this nanocomposite to market in as many ways as possible. This is the motivation for this study into induction motor design. Like the transformers that are utilizing HTX-012B's improved Steinmetz coefficients to reduce the size by employing higher driving frequencies, the hope is that this material will also allow for size reduction and efficiency improvement in induction motors.

4.2 METHOD OF TESTING

In this section, we present an overview of how we will approach reducing the motor size. All the concepts presented here will be explained in subsequent sections. Now that the material data has been entered into ANSYS Maxwell and validated, we are able to apply this material to motor designs within RMxpert; a motor simulation program within the ANSYS software package. RMxpert comes stock with example motor models that the company has created and are modeled after existing motors. To prove HTX-012B's benefits, we start with one of these

example motor models. Next, two new models are created; one with 2 poles, and one with a higher number of poles. HTX-012B will be applied to the stator core of each model. To achieve the same rotational speed, the model with more poles will have to be driven at a higher frequency. The rated voltage and the rated power output are the same for both motor models. Next, an optimization algorithm is run for the geometry of the higher pole motor. The optimization results are then applied to the motor, and the resulting machine operating parameters are compared to the 2 pole motor.

4.3 A BRIEF EXPLANATION OF MOTOR FUNDAMENTALS

Figure 24 depicts the equivalent circuit for an induction motor. R_1 and jX_1 make up the resistance and the inductance of the stator core and I_1 is the current through the stator coils. R_c is the stator core loss resistance, jX_m is the magnetizing inductance of the stator, and I_m is the magnetizing current. jX_2 and R_2 are the inductance and resistance of the rotor. Finally, Equation (4.1) describes s is the slip of the motor. Here, ω_{rm} is the angular frequency of the machine, and ω_{sync} is the synchronous angular frequency of the machine.

$$\omega_{rm} = (1 - s)\omega_{sync} \quad (4.1)$$

This figure will be used throughout this section to discuss what is happening within the motor [32].

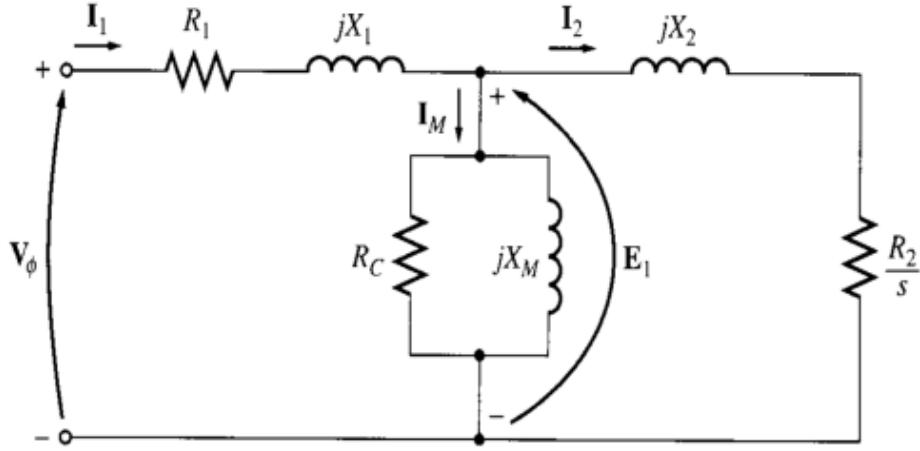


Figure 24. Equivalent Circuit for an AC Induction Motor

The mechanical output power for a motor is described by Equation (4.2) where τ is the torque

$$P_{mech} = \tau * \omega_{rm} \quad (4.2)$$

The resistance, R_2 , on the rotor side can be broken down into both the losses in the rotor and the output power of the machine as seen in Equation (4.3).

$$\frac{R_2}{s} = R_2 + \frac{R_2(1-s)}{s} \quad (4.3)$$

Equation (4.4) gives an alternative form of mechanical output power.

$$P_{mech} = \frac{3I_2^2 R_2(1-s)}{s} \quad (4.4)$$

Another relationship that is worthwhile to mention here is efficiency. The following derivation presents how efficiency relates to many of the aforementioned parameters.

$$n = P_{out}/P_{in} \quad (4.5.1)$$

$$n = \frac{P_{out}}{P_{out} + P_{losses}} \quad (4.5.2)$$

$$n = \frac{\frac{3I_2^2 R_2 (1-s)}{s}}{\frac{3I_2^2 R_2 (1-s)}{s} + 3I_2^2 R_2 + 3I_1^2 R_1 + 3I_m^2 R_C} \quad (4.5.3)$$

$$n = \frac{\frac{I_2^2 R_2 (1-s)}{s}}{\frac{I_2^2 R_2}{s} + I_1^2 R_1 + I_m^2 R_C} \quad (4.5.4)$$

What is important to take away from all this is that there is an intricate tie between the slip of the machine, the current through the rotor, and the output power, and the efficiency [32].

4.3.1 Rotation Speed and the Number of Poles

Motor rotational speed is governed by Equation (4.6)

$$RPM = \frac{120 * f}{N_p} \quad (4.6)$$

where RPM is rotations per minute, f is the driving frequency, and N_p is the number of poles. As the number of poles is increased for a given motor design, the driving frequency will have to be proportionally increased to keep the rotation speed the same.

4.3.2 Magnetizing Current, Flux, and the Number of Poles

To set up magnetic fields in the stator core, magnetizing current is required. This current is described by I_m in Figure 24. Flux travels through the stator core from the end of one magnetic pole to the other. As the number of poles in a motor increases, the flux has to travel less distance to get from one end of a pole to the other. However, this can lead to complications.

There is an inverse relationship between the number of poles and the necessary thickness or width of the return path in the stator core. If the thickness is not increased, flux crowding will occur and will diminish the motor's ability to produce torque; additionally the magnetizing current will also increase. This increases the full load current and therefore the primary I^2R losses as described by Equation (4.7).

$$I_1 = I_m + I_2 \quad (4.7)$$

In order to maintain the same output power, I_2 cannot diminish. Therefore, I_1 must increase to provide more magnetizing current. As the magnetizing current increases, the power factor of a motor decreases. See Figure 25 for a depiction of drop in power factor as the number of poles rise. Figure 26 provides a comparison between a 2 pole and 4 pole motor.

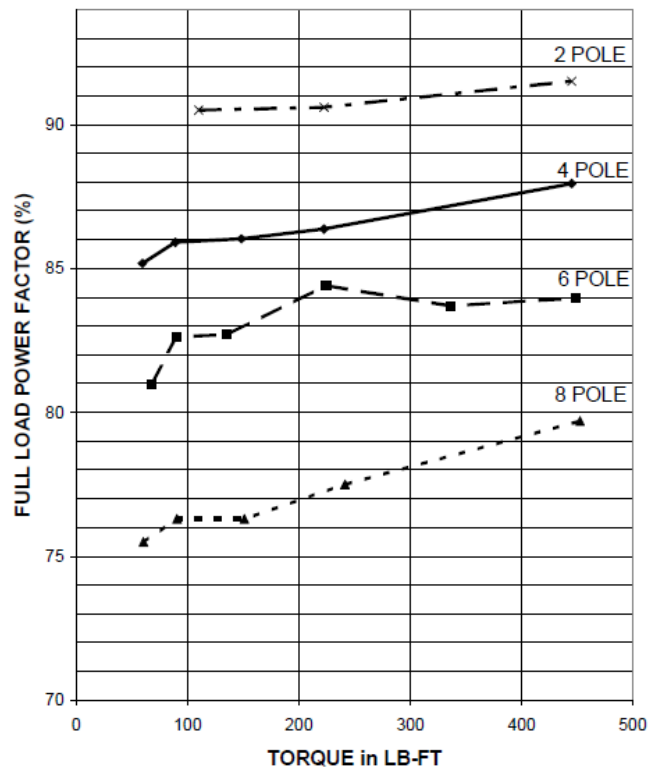
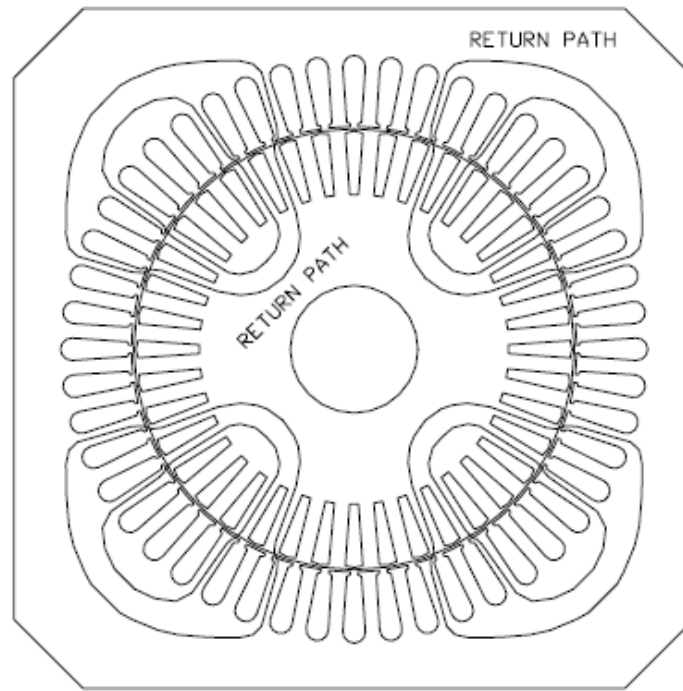
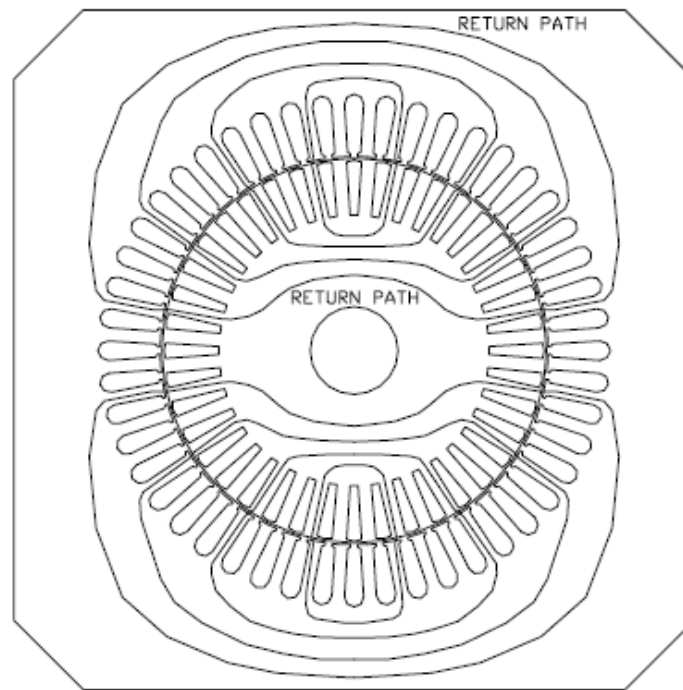


Figure 25. Typical Full Load Power Factors of Fixed Speed AC Motors 0



(a) 4 pole



(b) 2 pole

Figure 26. AC Induction Motor Cross Section for a 2 Pole versus a 4 Pole Design 0

4.3.3 Core (Iron) Losses

Induction motor core losses are made up of two main components: hysteretic losses and eddy current losses. Hysteretic loss will vary almost linearly with increases in frequency, while the eddy current loss component varies by close to the square of the stator frequency. These loss components are based on the properties of the stator core material. HTX-012B has low loss coefficients for these two kinds of losses which could make it ideal for use in higher frequency applications [32]. This harkens back to the earlier study of the Steinmetz coefficients with core loss versus frequency for HTX 012B.

4.4 ROTOR MATERIAL FOR TESTS

The motor models that come stock in the ANSYS RMxpert library employ a material named M19 24G. This material has values for the loss coefficients that are described in section 3.3.2. However, the frequency range at which these loss coefficients were calculated is unknown. Therefore, a new material for the rotor ought to be imputed so as to be sure that the loss coefficients are valid for the tested frequency range.

Reference 0 presents a study of an amorphous stator core motor and examines its performance characteristics as compared to an electric steel, M600-50A. The core loss vs. frequency data was given in reference 0 and can be seen in Figure 27. The dashed line represents the M600-50A while the solid line represents their new amorphous material. The calculated loss coefficients are contained in Table 12. The rest of the material data for M600-50A was obtained from manufacturers' sites, references 0 and 0, and can also be seen in Table

12. This material data is valid for our studies as the core loss versus frequency is tested up to 2 kHz.

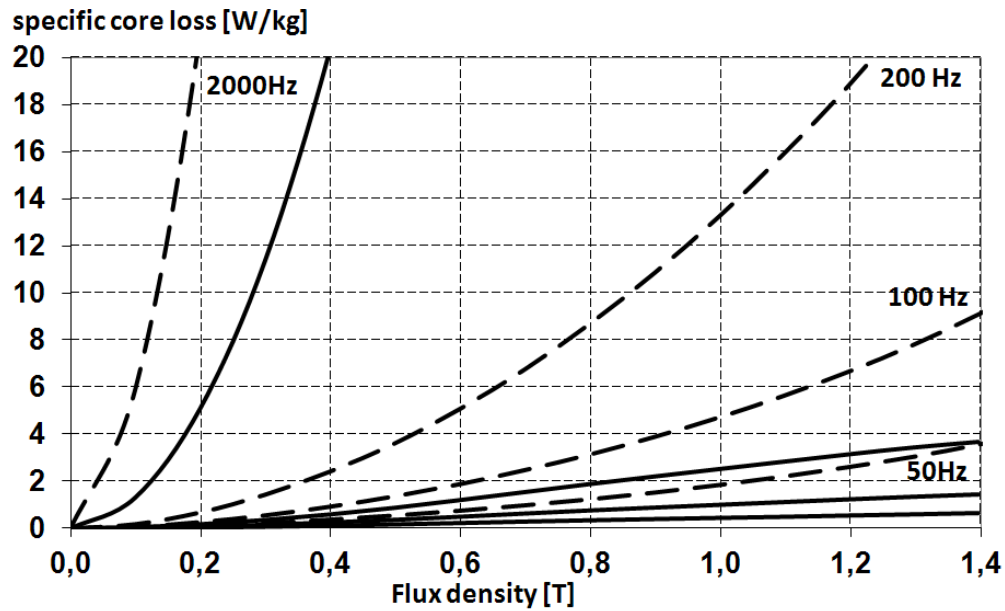


Figure 27. Core Loss vs. Frequency for M600-50A

Table 12. Material Data for M600-50A

M600-50A		
Bulk Conductivity	33333333	Siemens/m
Kh	0.0368	
Kc	7.9463	
Ke	0.000802	
Mass Density	7750	kg/m ³

4.5 NEW DATA FOR HTX-012B

Because motors are typically run well below 10 kHz, it was important to have loss coefficients for HTX-012B valid for this range. For this reason, the medium, solid core was tested again at Spang Magnetics to obtain core loss versus frequency data at lower frequencies that are applicable for motor tests. This experimental data is contained in Table 13 and the loss coefficients are displayed in Figure 28. This material data sheet was used for the following motor tests.

The reader may notice that there is a slight difference between the loss coefficients for this data sheet displayed in Figure 28 and the data sheet displayed in Figure 15. This is because HTX 012B has slightly different loss properties above and below 10 kHz. The reasons for this are beyond the scope of this thesis and will not be discussed.

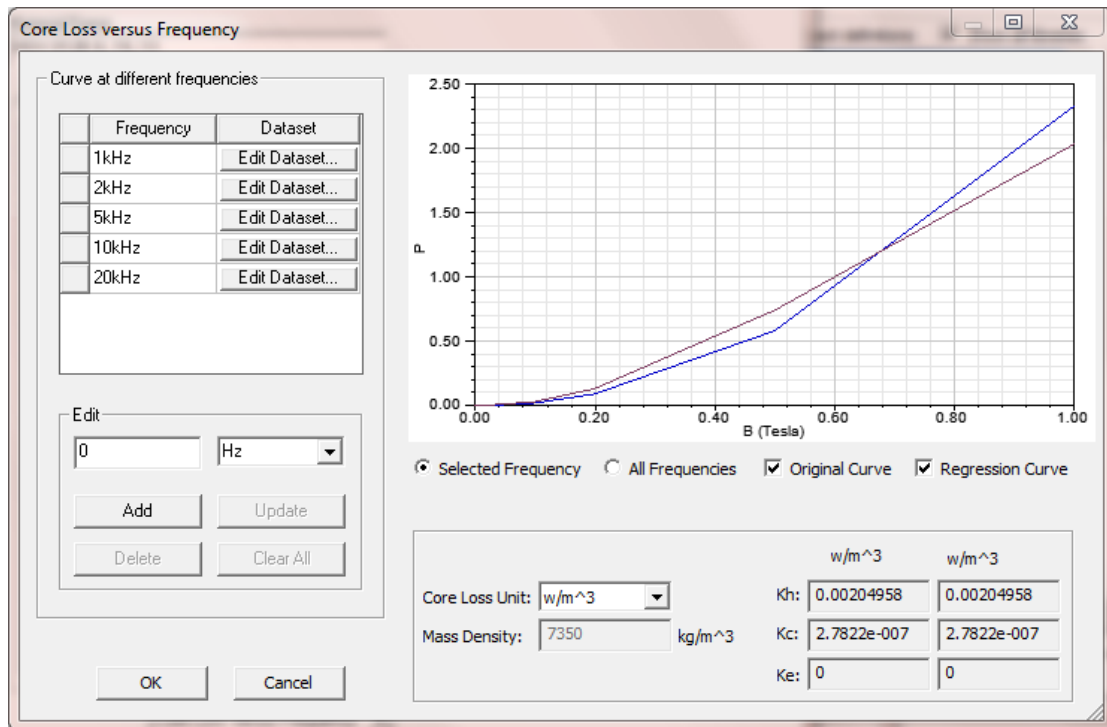


Figure 28. Material Data Input Screen for Core Loss vs. Frequency

Table 13. Loss vs. Frequency Data for Solid Medium Core -- 1 kHz to 20 kHz

B (T)	1 kHz	2 kHz	5 kHz	10 kHz	20 kHz
0.1	0.033	0.0748	0.2508	0.5456	1.3552
0.2	0.1342	0.3344	0.935	1.9976	5.7464
0.5	0.7414	1.6522	4.7256	12.1022	36.443
1	2.0306	5.0424	17.7738	47.8698	152.77

4.6 2 POLE VERSUS 16 POLE MOTOR TEST

4.6.1 2 Pole Test

The first motor model tested comes in the ANSYS Maxwell 16 RMxpert example library and is named, “yz200-24.” This motor originally has 24 poles, a rated voltage of 380V, and a rated output power of 3.2kW. Figure 29 shows a 2D model of the stator and rotor. Table 14 gives the geometric values of the stator and rotor. Figure 30 provides an image of the slot and tooth geometry for the stator and rotor respectively, while Table 15 provides the geometric values.

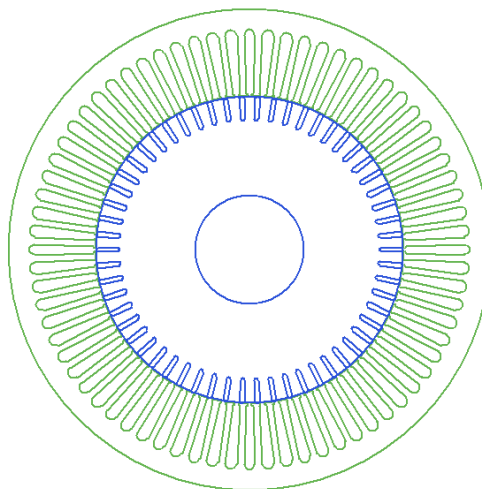


Figure 29. 24 Pole (Original) Induction Motor

Table 14. Values for Rotor and Stator Geometries of 24 Pole (Original) Motor

	Stator	Rotor	
Outer Diameter	327	209.2	(mm)
Inner Diameter	210	75	(mm)
Length	280	280	(mm)
Stacking Factor	0.92	0.92	
Number of Slots	72	58	

Table 15. Values for Rotor and Stator Slot Geometries of 24 Pole (Original) Motor

	Stator Slot	Rotor Slot	
Hs0	0.8	0.5	(mm)
Hs01	NA	0	(mm)
Hs1	0.52	0.66	(mm)
Hs2	39.48	14.34	(mm)
Bs0	3	1	(mm)
Bs1	4.8	3.3	(mm)
Bs2	8.2	3.3	(mm)

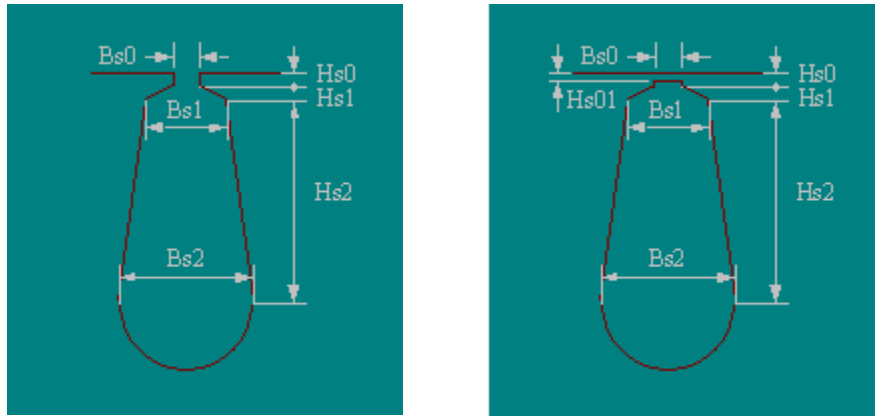


Figure 30. Rotor and Stator Geometry Variables

This motor's original geometry is not altered, and the operating voltage is kept at 380V. Its pole number is changed to 2, and its stator winding configuration is changed to whole-coiled. Motor winding is an integral part of the motor design as it can affect harmonics, the flux through

the core, and many other aspects of the design. Whole-coiled winding was selected in order to maintain a constant design parameter for both the 2 pole and the 8 pole.

Given that the designed driving frequency is 50Hz, the rated speed is listed at just under 3000 RPM (at 2900 RPM). This is done so that RMXprt will not analyze the motor above the actual rotational speed, which will be less than synchronous speed. From here an analysis of this motor design is run. The rated performance, rated electrical data, and material consumption is recorded and will be discussed and compared after the 16 pole motor is presented.

4.6.2 16 Pole Test

A new motor model is then created with all the same inputs as the 2 pole design. The pole number is changed to 16 and the driving frequency is changed to 400Hz to maintain the mechanical speed of 3000 RPM. At this point, new variables are assigned to certain aspects of the motor geometry. The variables listed in Table 16 and Table 17 were selected based on the magnitude of the impact they would have on the operational characteristics. As a point of order, “S” is a scaling variable.

Table 16. Values for Rotor and Stator Geometries of 16 Pole Motor

	Stator	Rotor	
Outer Diameter	ODS*S	ODR*S	(mm)
Inner Diameter	210*S	75*S	(mm)
Length	L*S	L*S	(mm)
Stacking Factor	0.92	0.92	
Number of Slots	72	58	

Table 17. Values for Rotor and Stator Slot Geometries of 16 Pole Motor

	Stator Slot	Rotor Slot	
Hs0	$0.8*S$	$0.5*S$	(mm)
Hs01	NA	0	(mm)
Hs1	$0.52*S$	$0.66*S$	(mm)
Hs2	$Hs_{ii}S$	$Hs_{ii}R$	(mm)
Bs0	$3*S$	$1*S$	(mm)
Bs1	$4.8*S$	$0.33*S$	(mm)
Bs2	$8.2*S$	$0.33*S$	(mm)

At this point, an optometric study is set up to find a geometry that matches the output parameters of the 2 pole design. This study is conducted by changing the variables listed in Table 18. The limits for the variables of the optometric study are also listed in Table 18 and all units are in mm.

Table 18. Variable and Limits for Optometric Study of 16 Pole Motor

	Min	Max	Min Focus	Max Focus
Hs_{ii}R	2	21.51	2	21.51
Hs_{ii}S	2	40	2	40
L	100	420	100	420
ODR	205	209.9	205	209.9
ODS	310	550	310	550
S	0.4	1	0.4	1

More slot variables are not utilized so as to reduce the solve time. A sequential nonlinear algorithm is employed for this optometric study. The constraints for the optometric study are listed in Table 19.

Table 19. Optometric Study Calculations for 16 Pole Motor.

	Condition	Goal	Weight
Efficiency Parameter	\geq	70	1
Power Factor Parameter	\geq	0.8	1
Slot Fill Factor Parameter	\leq	90	2
Output Power Parameter	\geq	3190	2

The goal for the efficiency was selected based in the rated performance of the 2 pole motor. As discussed in 4.3.2, we can expect to see a decrease in the power factor. Therefore, a goal was set to attempt to design for a higher power factor. Finally, the slot fill factor determines the percentage of the slot that is taken up by the conductors. If this value is not specified, the optometric analysis will provide a motor design with a fill factor above 100% which is not attainable.

4.6.3 Results of 2 Pole versus 16 Pole Test

The result of the optometric analysis for the 16 pole motor is shown in Table 20 and Table 21. The rated performance, rated electrical data, and material consumption for the 2 pole and 16 pole motors are contained in Table 22. There is an 85% reduction in size and an 82% reduction in weight for the optimized 16 pole motor. While the output power, rated torque, and efficiency are all relatively the same, there is a 55% reduction in power factor. We can also see from Figure 31 and Figure 32 that there is a reduction in the maximum torque for the motor from 17.13 N-m to 11.68 N-m; however, rated torque remains the same.

Table 20. Results of Optimization for Rotor and Stator Geometry - 16 Pole

	Stator	Rotor	
Outer Diameter	239.42	160.23	(mm)
Inner Diameter	162.07	57.88	(mm)
Length	78.33	78.33	(mm)
Stacking Factor	0.92	0.92	
Number of Slots	72	58	

Table 21. Results of Optimization for Rotor and Stator Slot Geometry - 16 Pole

	Stator Slot	Rotor Slot	
Hs0	0.61	0.38	(mm)
Hs01	NA	0	(mm)
Hs1	0.4	0.5	(mm)
Hs2	27.18	7.75	(mm)
Bs0	2.31	0.77	(mm)
Bs1	3.7	2.54	(mm)
Bs2	6.32	2.54	(mm)

Table 22. Rated Performance Characteristics for 2 Pole vs. Optimized 16 Pole Motor

	2 Pole Motor	16 Pole Motor	
	Rated performance		
Stator Ohmic Loss	115.019	115.12	W
Rotor Ohmic Loss	259.82	254.95	W
Iron-Core Loss	0.000345	0.000712	W
Output Power	3200.13	3200.23	W
Input Power	3719.44	3714.88	W
Efficiency	86.03	86.14	%
Power Factor	0.941	0.4211	
Rated Torque	10.99	10.97	N-m
Rated Speed	2780.33	2784.17	RPM
Rated Slip	0.0732	0.0719	
	Rated Electric Data		
Stator Phase Current	5.97926	13.34	A
Magnetizing Current	0.1582	7.24	A
Rotor Phase Current	5.959	9.14	A
	Material Consumption		
Total Net Weight	139.554	24.537	kg
Total Size	0.023514915	0.003526459	m ³

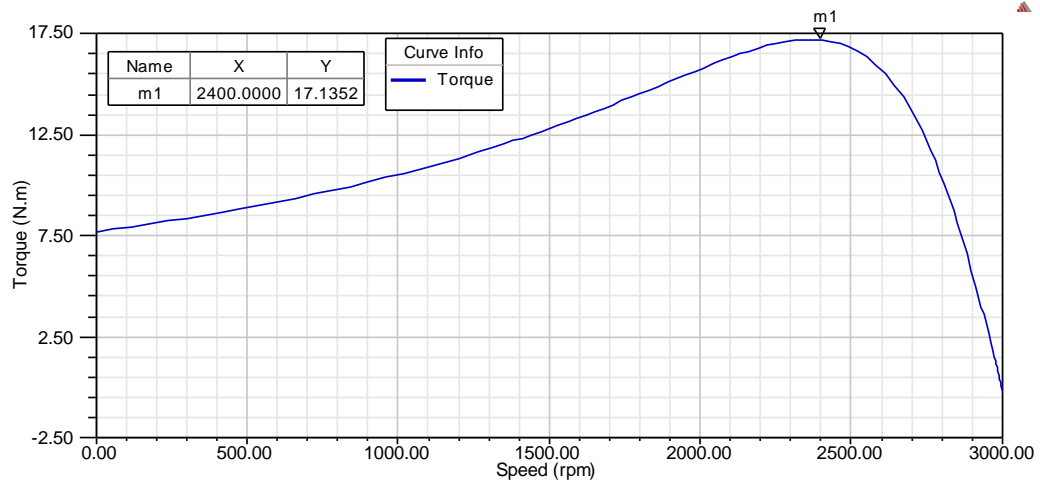


Figure 31. Torque vs. Speed Curve for 2 Pole Motor

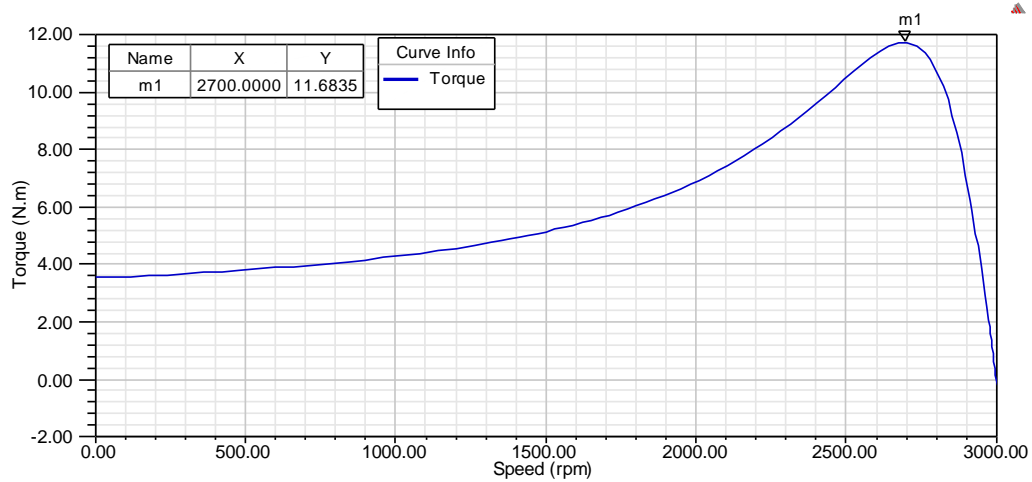


Figure 32. Torque vs. Speed Curve for Optimized 16 Pole Motor

To observe the flux crowding effect that was described in 4.3.2, Maxwell 2D models of both motors are created and displayed in Figure 33 and Figure 34. We can see from these that the 2 pole design has flux flowing out of the right side of the motor, splitting (because there are two poles) and flowing around the top and bottom of the motor. In the 16 pole motor, we can distinctly count 8 poles across the top section of the motor. In addition, the maximum Webers per meter for the 2 pole design is $1.1\text{e-}2$ while, the maximum flux for the 16 pole design is 2.09e-

2. This confirms the statement that as flux crowding increases, torque and power factor both decrease.

It is worth noting that in order to preserve the integrity of the original model, the rated voltage was not changed from 380V. Because the original model was made using M19 24G, a material with a saturation level well above that of HTX 012B (2.1[T] vs. 1.2[T]), there is localized saturation occurring in both models. This can be seen in Figure 35 and Figure 36. By lowering the voltage, core loss will be reduced. Lowering the voltage also lowers the flux by Equation (4.8). Therefore, if this is done, the optimal output power would need to be reassessed;

$$V = \omega * \varphi * N_{poles} * \cos(\omega t) \quad (4.8)$$

where V is the applied voltage, ω is the rotating frequency, and φ is the flux 0.

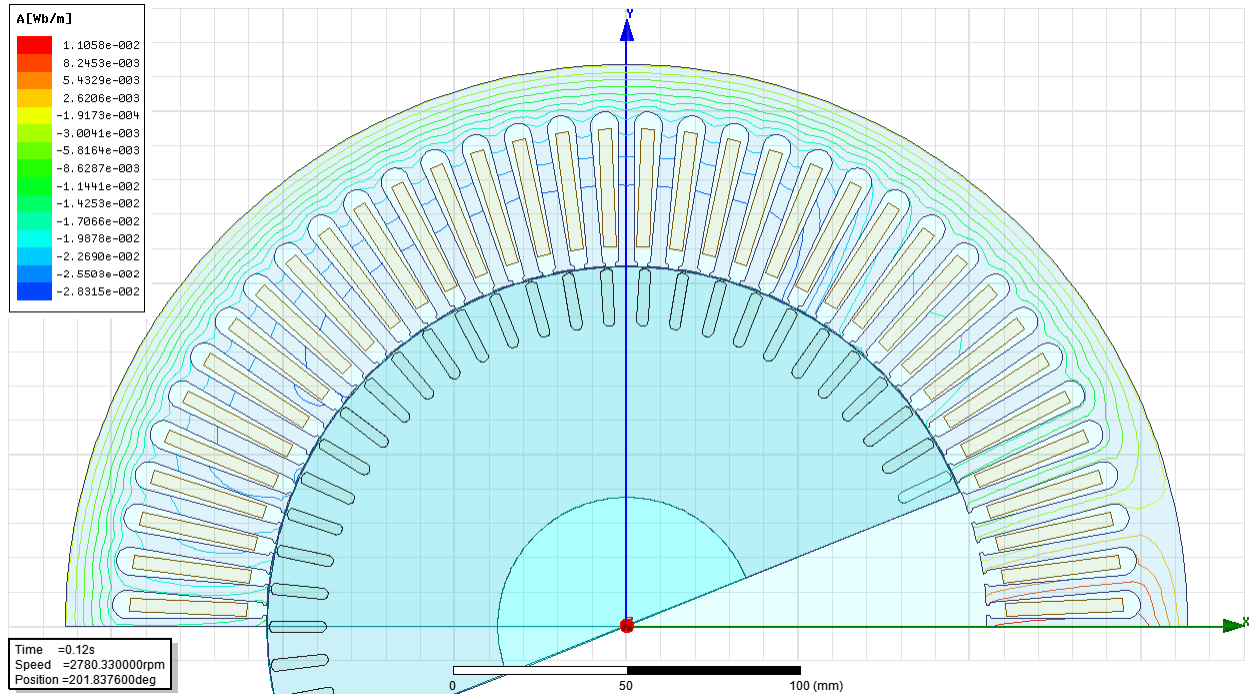


Figure 33. Flux Lines for 2 Pole Motor

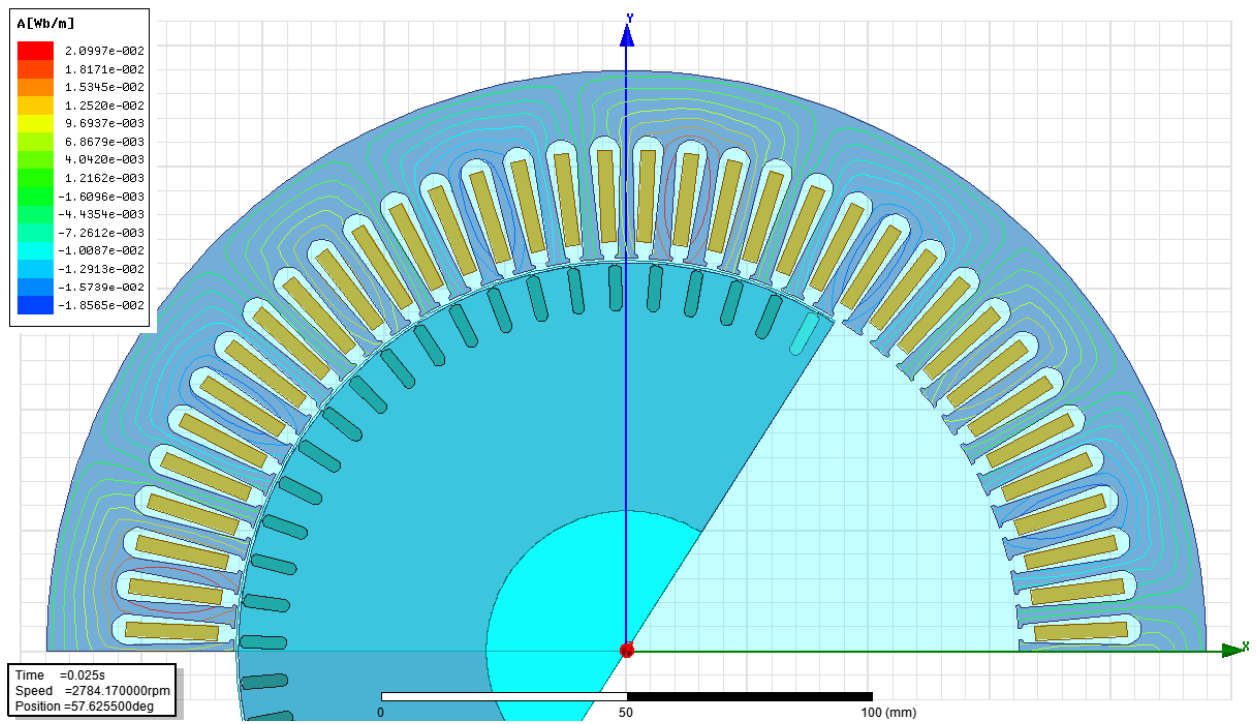


Figure 34. Flux Lines for Optimized 16 Pole Motor

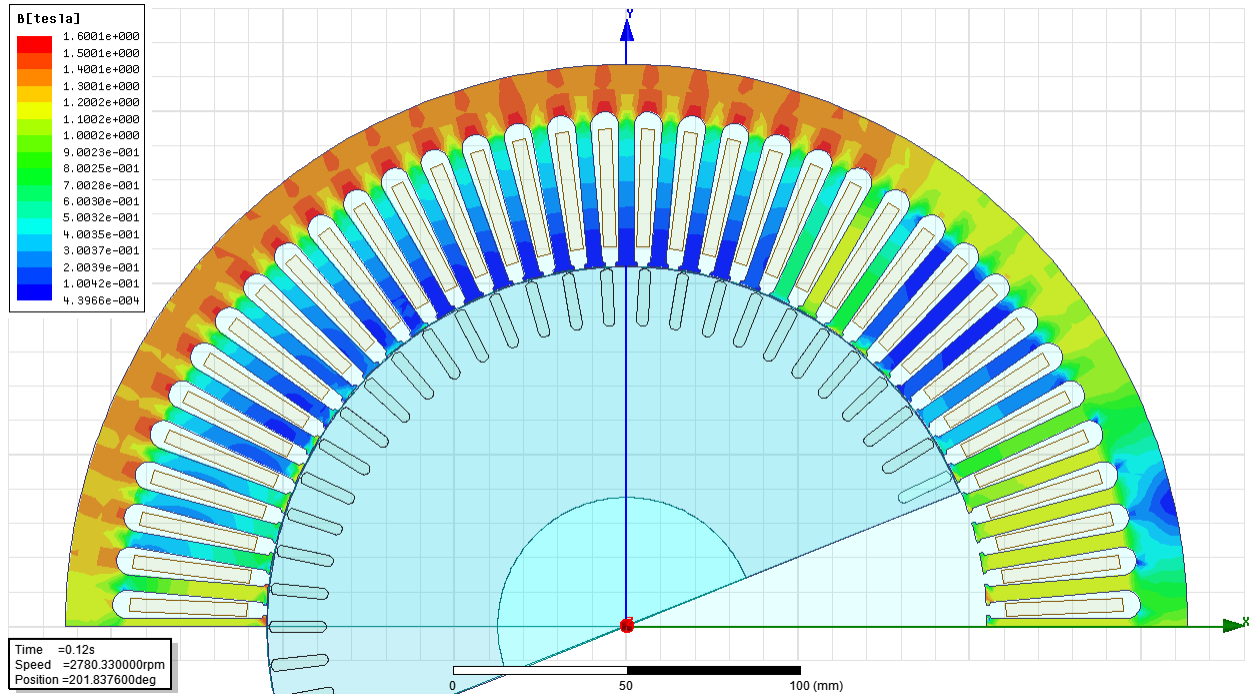


Figure 35. Magnetic Field Strength for 2 Pole Motor

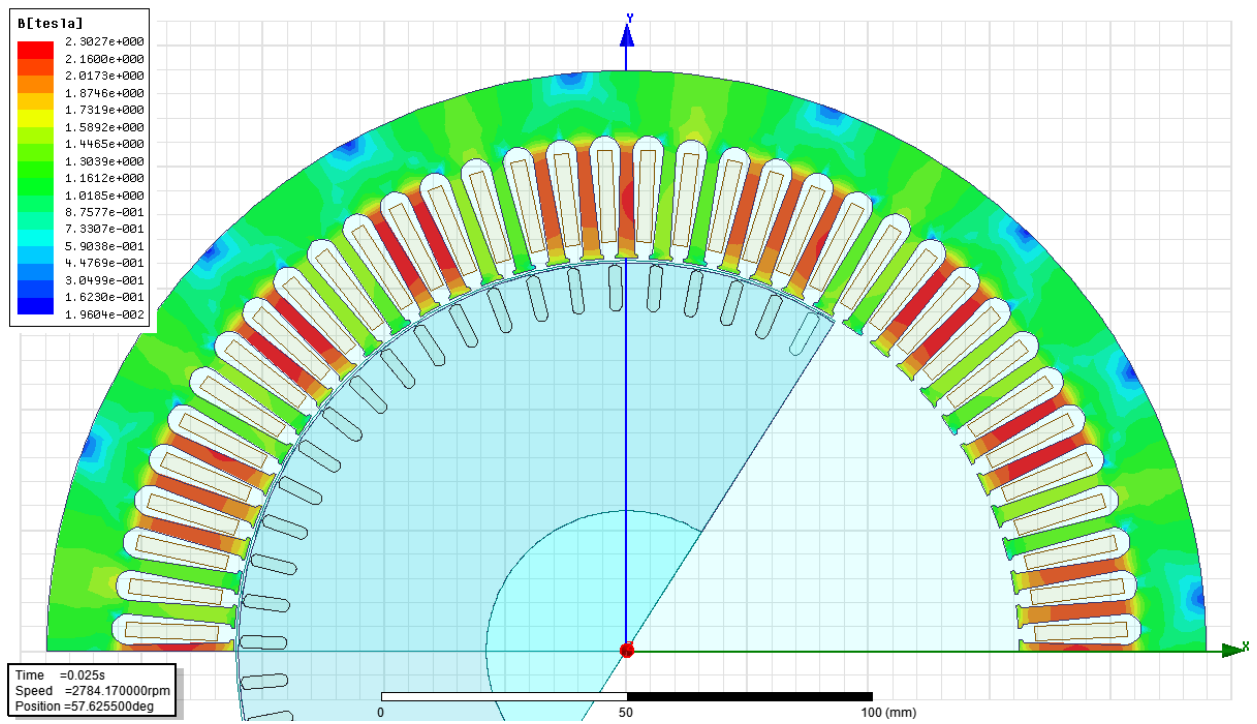


Figure 36. Magnetic Field Strength for Optimized 16 Pole Motor

4.7 2 POLE VERSUS 8 POLE MOTOR TEST

4.7.1 2 Pole Test

The second motor model tested also comes stock in the ANSYS Maxwell 16 RMXprt example library and is named, “yzd132-8.” This motor originally has 8 poles, a rated voltage of 380V, and a rated output power of 1.3kW. Figure 37 shows a 2D model of the stator and rotor.

Table 23 gives the geometric values of the stator and rotor. Figure 38 provides an image of the slot and tooth geometry for the stator and rotor respectively, while Table 24 provides the geometric values.

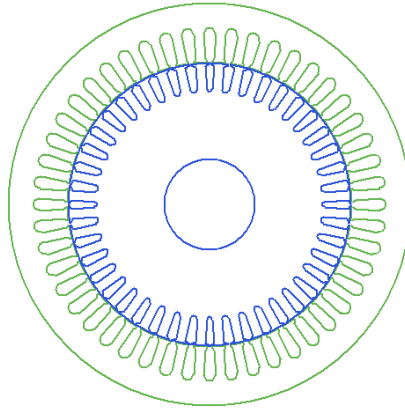


Figure 37. 8 Pole (Original) Motor

Table 23. Values for Rotor and Stator Geometries of 8 Pole (Original) Motor

	Stator	Rotor	
Outer Diameter	210	147.3	(mm)
Inner Diameter	148	48	(mm)
Length	250	250	(mm)
Stacking Factor	0.92	0.92	
Number of Slots	48	44	

Table 24. Values for Rotor and Stator Slot Geometries of 8 Pole (Original) Motor

	Stator Slot	Rotor Slot	
Hs0	0.8	0.5	(mm)
Hs01	NA	0	(mm)
Hs1	1.05	1.2	(mm)
Hs2	12.9	12	(mm)
Bs0	2.8	1	(mm)
Bs1	4.9	5.2	(mm)
Bs2	6.7	3.5	(mm)

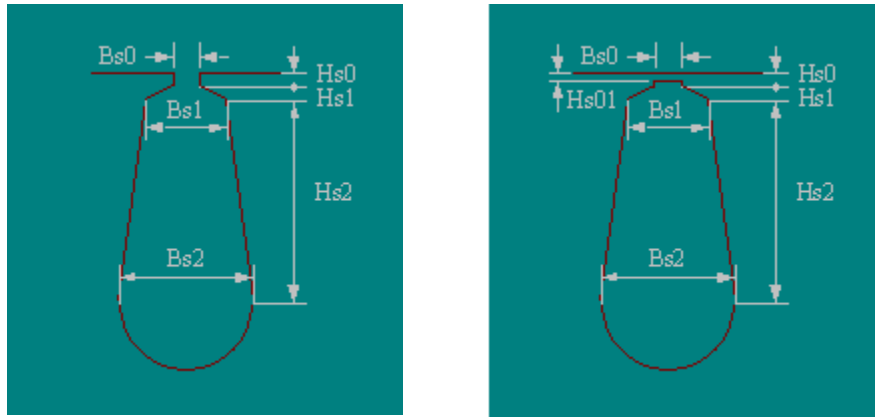


Figure 38. Rotor and Stator Geometry Variables

This motor's original geometry is not altered, and the operating voltage is kept at 380V. Its pole number is changed to 2, and, as before, its stator winding configuration is changed to whole-coiled. Given that the designed driving frequency is 50Hz, the rated speed is listed at just under 3000 RPM (at 2800 RPM). This is done so that RMxpert will not analyze the motor above the actual rotational speed which will be less than synchronous speed. From here an analysis of this motor design is run. The rated performance, rated electrical data, and material consumption is recorded and will be discussed and compared after the 8 pole motor is presented.

4.7.2 8 Pole Test

A new motor model is then created with all the same inputs as the 2 pole design. The pole number is changed to 8 and the driving frequency is changed to 200Hz to maintain the mechanical speed of 3000 RPM. At this point, new variables are assigned to certain aspects of the motor geometry. These variables are listed in Table 25 and Table 26 and were selected based on the magnitude of the impact they would have on the operational characteristics. As a point of order, “S” is a scaling variable.

Table 25. Values for Rotor and Stator Geometries of 8 Pole Motor

	Stator	Rotor	
Outer Diameter	ODS*S	ODR*S	(mm)
Inner Diameter	148*S	75*S	(mm)
Length	L*S	L*S	(mm)
Stacking Factor	0.92	0.92	
Number of Slots	48	44	

Table 26. Values for Rotor and Stator Slot Geometries of 8 Pole Motor

	Stator Slot	Rotor Slot	
Hs0	0.8*S	0.5*S	(mm)
Hs01	NA	0	(mm)
Hs1	1.05*S	1.2*S	(mm)
Hs2	HsiiS*S	HsiiR*S	(mm)
Bs0	2.8*S	1*S	(mm)
Bs1	4.9*S	5.2*S	(mm)
Bs2	6.7*S	3.5*S	(mm)

At this point, an optometric study is set up to find a geometry that matches the output parameters of the 2 pole design. The limits for the variables of the optometric study are listed in Table 27 and all units are in mm.

Table 27. Variable and Limits for Optometric Study of 8 Pole Motor

	Min	Max	Min Focus	Max Focus
HsiR	4	14	4	14
HsiS	4	14	4	14
L	125	375	125	375
ODR	190	210	190	210
ODS	137	147.9	137	147.9
S	0.4	1	0.4	1

More slot variables are not utilized so as to reduce the solve time. A sequential nonlinear algorithm is employed for this optometric study. The constraints for the study are listed in Table 28.

Table 28. Optometric Study Calculations for 8 Pole Motor.

	Condition	Goal	Weight
Efficiency Parameter	\geq	77	1
Power Factor Parameter	\geq	0.93	1
Slot Fill Factor Parameter	\leq	79	1

The goal for the efficiency was selected based on the performance of the 2 pole motor. As discussed in before, we can expect to see a decrease in the power factor. Therefore, a goal was set to attempt to optimally design for a higher power factor. Finally, the slot fill factor was specified so as to prevent the analysis from giving unattainable results of over 100%.

4.7.3 Results of 2 Pole versus 8 Pole Test

The result of the optometric analysis for the 8 pole motor test are displayed in Table 29 and Table 30. The rated performance, rated electrical data, and material consumption for the 2

pole and 8 pole motors are contained in Table 31. There is a 56% reduction in size and a 57% reduction in weight for the optimized 8 pole motor. While the output power, rated torque, and efficiency are all relatively the same, there is a 7.6% reduction in power factor. Figure 39 and Figure 40 show that there is a reduction in the maximum torque for the motor from 40 N-m to 37.2 N-m; however, rated torque remains the same.

Table 29. Results of Optimization for Rotor and Stator Geometry - 8 Pole

	Stator	Rotor	
Outer Diameter	196.62	147.9	(mm)
Inner Diameter	148	48	(mm)
Length	125	125	(mm)
Stacking Factor	0.92	0.92	
Number of Slots	48	44	

Table 30. Results of Optimization for Rotor and Stator Slot Geometry - 8 Pole

	Stator Slot	Rotor Slot	
Hs0	0.8	0.5	(mm)
Hs01	NA	0	(mm)
Hs1	1.05	1.2	(mm)
Hs2	14	8.553	(mm)
Bs0	2.8	1	(mm)
Bs1	4.9	5.2	(mm)
Bs2	6.7	3.5	(mm)

Table 31. Rated Performance Characteristics for 2 Pole vs. Optimized 8 Pole Motor

	2 Pole Motor	8 Pole Motor	
	Rated performance		
Stator Ohmic Loss	21.965	9.87	W
Rotor Ohmic Loss	29.444	10.4	W
Iron-Core Loss	0.000564	0.0011288	W
Output Power	1300.1	1299.3	W
Input Power	1519.94	1490.02	W
Efficiency	85.53	87.1997	%
Power Factor	0.967	0.8931	
Rated Torque	4.222	4.16534	N-m
Rated Speed	2940.52	2978.72	RPM
Rated Slip	0.01982	0.007	
	Rated Electric Data		
Stator Phase Current	1.3668	1.451	A
Magnetizing Current	0.2922	0.4377	A
Rotor Phase Current	1.329	1.3378	A
	Material Consumption		
Total Net Weight	54.9871	23.448	kg
Total Size	0.008659015	0.00379538	m^3

Figure 39. Torque vs. Speed Curve for 2 Pole Motor

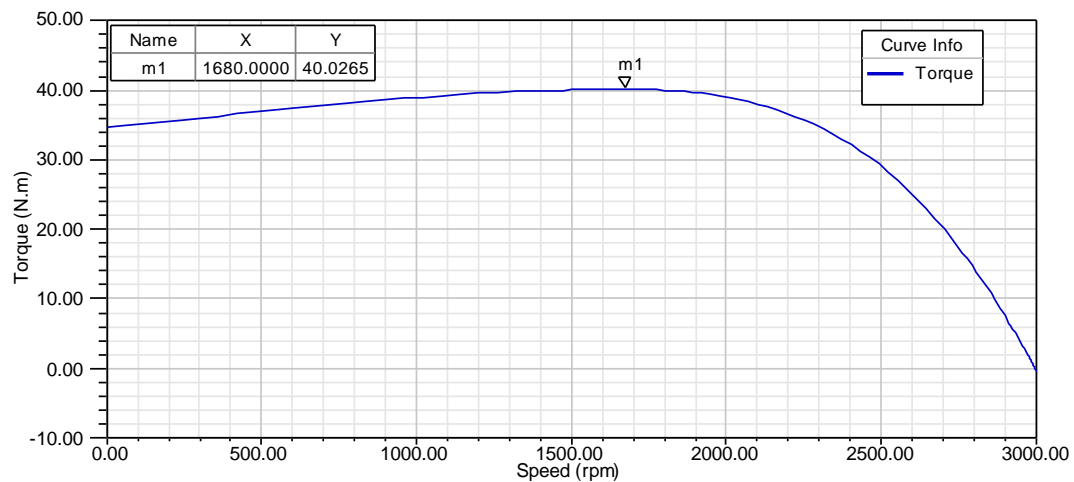
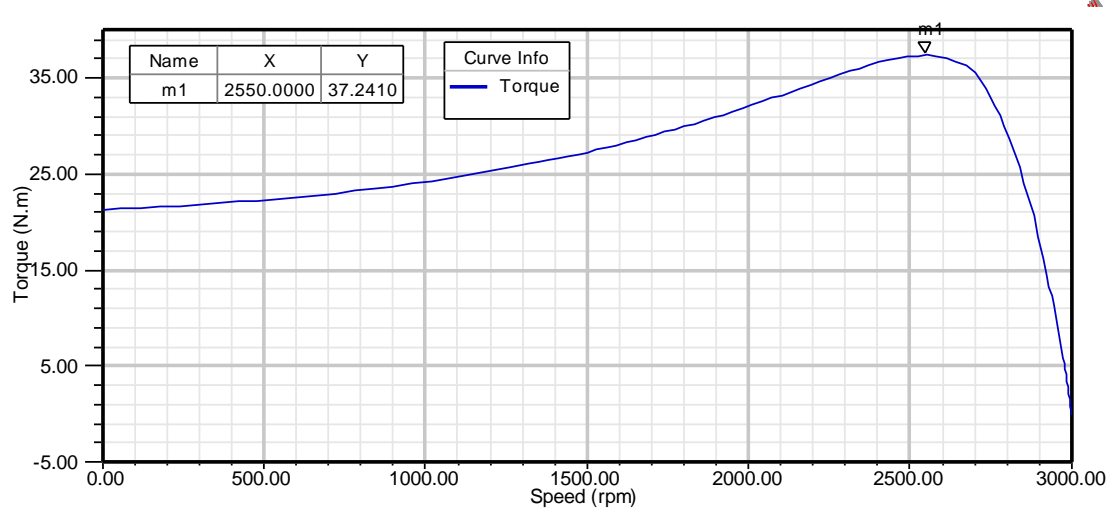


Figure 40. Torque vs. Speed Curve for Optimized 8 Pole Motor



To observe the flux crowding effect that was described in 4.3.2, Maxwell 2D models of both motors are displayed in Figure 41 and Figure 42. As before, we can see the 2 pole design has flux flowing out of the right side of the motor and splitting. A quarter view of the 8 pole motor is displayed in Figure 42 and we can see 2 distinct poles. The difference in maximum flux between the 2 pole and 8 pole designs is $2.6\text{e-}3$ Wb/m while the difference between the 2 pole and 16 pole motors is $9.9\text{e-}3$. With this reduced difference in flux, we only see a 7.6% drop in power factor between the 2 pole and the 8 pole motor. In addition, because of the reduced flux crowding, we do not see as much of a loss of torque.

As with the first two models, there is also localized saturation that can be seen in Figure 43 and Figure 44. This again is due to the fact that the motor was originally designed to utilize a material with a higher level of saturation.

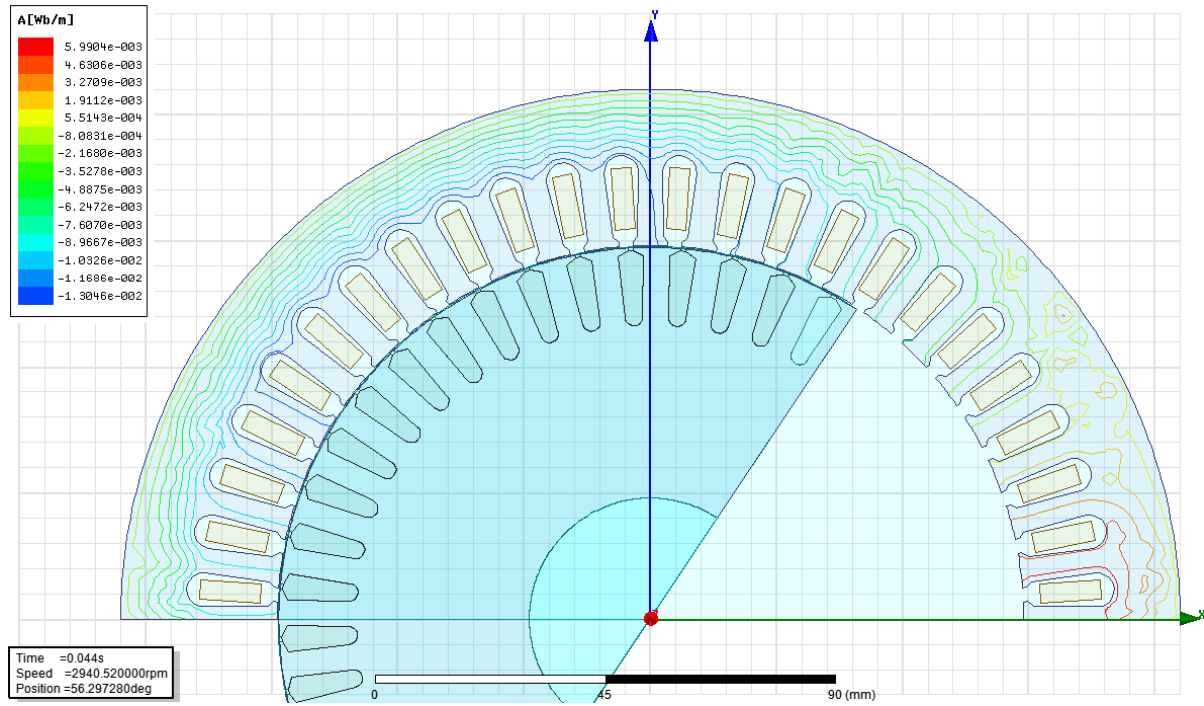


Figure 41. Flux Lines for 2 Pole Motor

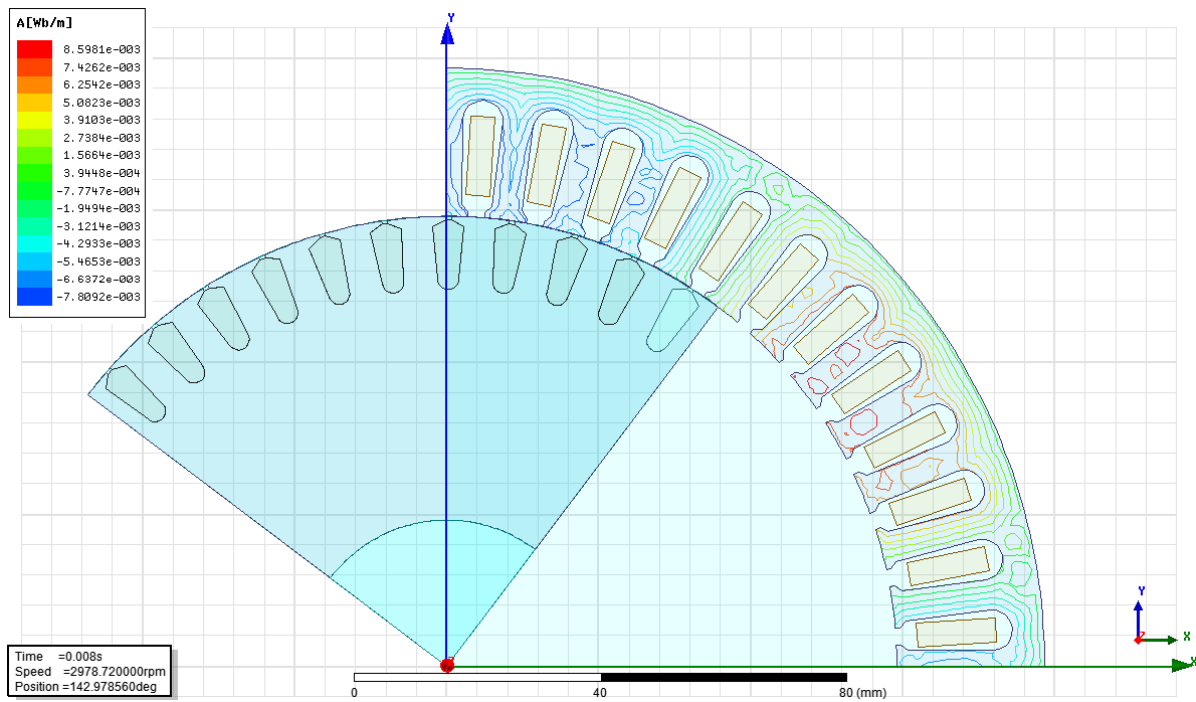


Figure 42. Flux Lines for Optimized 8 Pole Motor

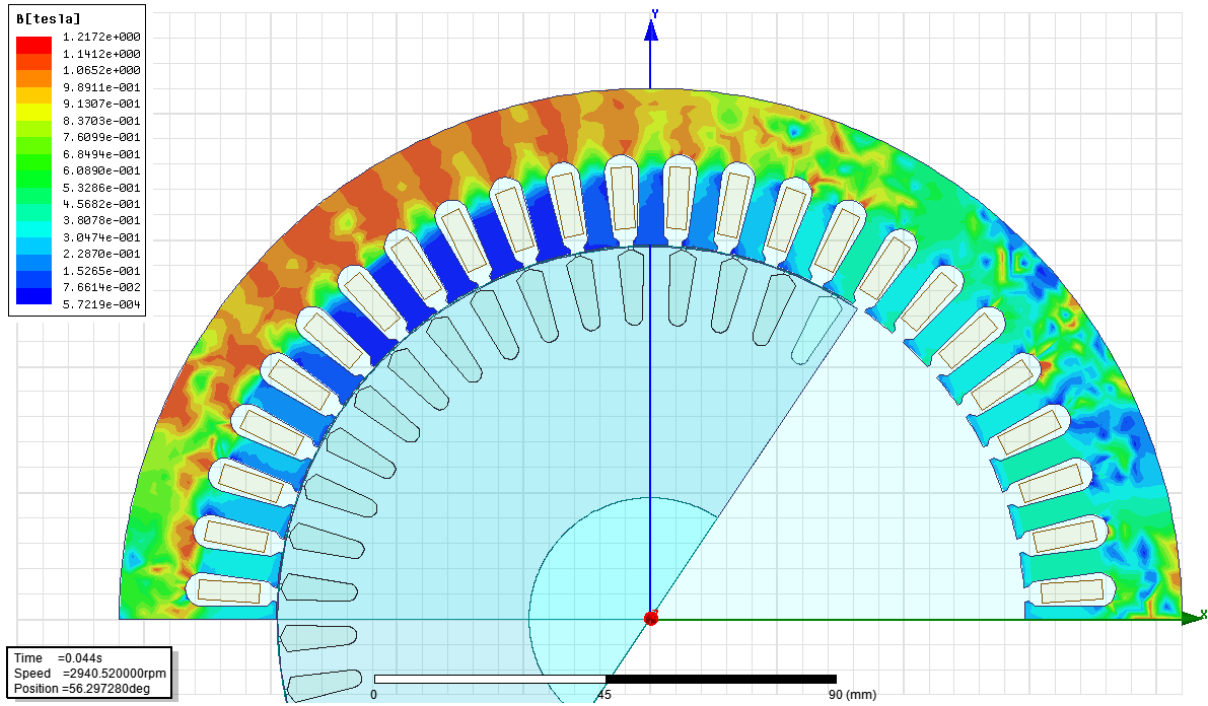


Figure 43. Magnetic Field Strength for 2 Pole Motor

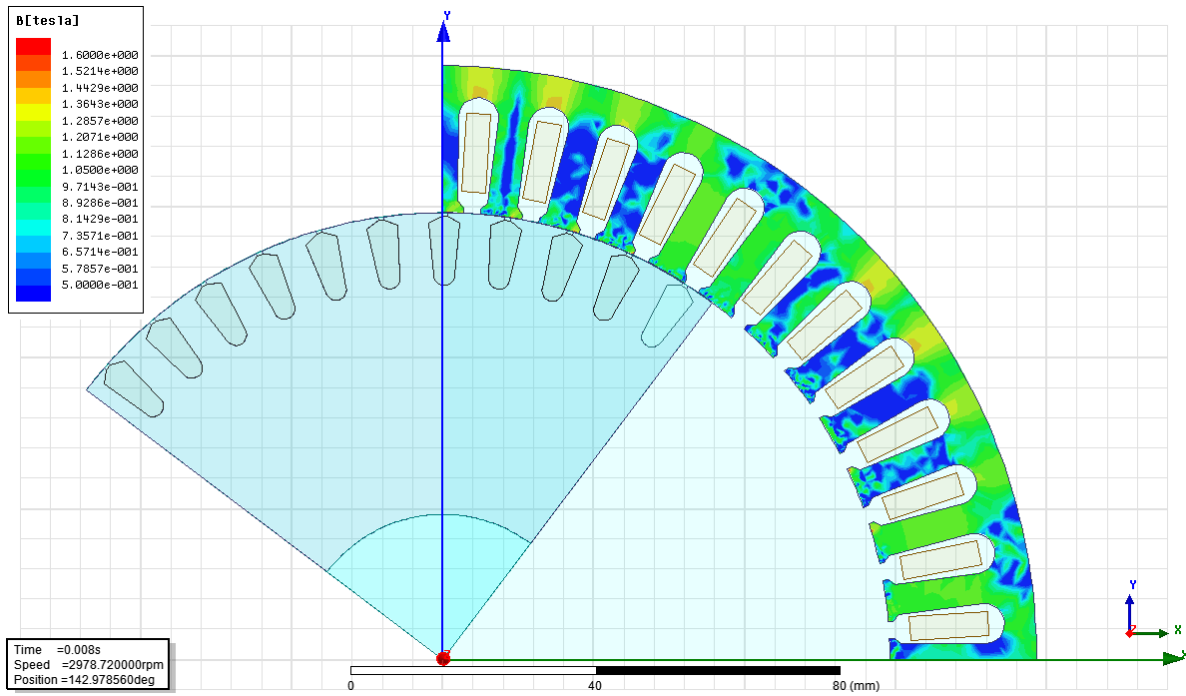


Figure 44. Magnetic Field Strength for Optimized 8 Pole Motor

4.8 CONCLUSIONS

Through the study of these two motor models, we have seen that, by employing HTX 012B, size reductions can be achieved with higher driving frequencies and higher number of poles. This increased frequency does not come with a loss in efficiency, but in fact, the opposite is true. With the 2 pole versus 8 pole motor study, we see a 2% increase in efficiency; however, this size reduction comes at the cost of power factor and torque.

With the 2 pole versus 16 pole study, we saw a difference of $9.9\text{e-}3$ Wb/m with a drop in maximum torque of roughly 32%. The 2 pole versus 8 pole study had a difference of $2.6\text{e-}3$ Wb/m and a drop in max torque of 7%. This shows that proper management of flux crowding has a drastic effect on the maximum torque when increasing the driving frequency and the number of poles. It must again be noted that the rated torque did not change for any motor model.

Two large concerns with HTX 012B also must be addressed here. The first is that HTX 012B has a saturation level that is lower than most electric steels. The operating conditions for these motors were obviously not designed for HTX 012B as there was localized saturation occurring for all models. When designing any motor, one must consider the saturation level of the material that is being utilized so as to ensure that the motor does not overheat and reduce its lifetime.

The second is that HTX 012B is relatively brittle compared to electric steels. Therefore it does not lend itself to rotor applications where there will be shearing stresses. Its ductility is especially important to consider when the motor may be used in an environment with external stresses on the stator.

5.0 FUTURE WORK

Because HTX 012B exhibits lower losses at higher frequencies, there may be benefits to using this material in induction motors that are driven by variable frequency drives. In V.F.D. applications, high frequency harmonics are generated due to pulse width modulation. In the following months, I will be conducting simulations studies of neutral point clamp converter utilizing ANSYS Simplorer.

Simplorer offers the ability to import motor models that are generated by RMxpert into the circuit model. With this ability, these simulations will be utilized to examine the core loss due to harmonics for the motor models that were presented in this thesis. In addition, I will study the differences in core loss for motors whose stator cores are made of HTX 012B vs. other materials such as M600-50A.

BIBLIOGRAPHY

- [1] R. Ram, “Power Electronics”, *ARPA-E Innovation Summit Pre-Summit Workshop*, (2010), Oxon Hill, MD.
- [2] A. Leary, P.R. Ohodnicki and M.E. McHenry, “Soft Magnetic Materials in High Frequency, High Power Conversion Applications”, *Journal of Metals*, 2012.
- [3] W Kramer, S Chakraborty, B Kroposki, and H Thomas. Advanced Power Electronic Interfaces for Distributed Energy Systems Part 1: Systems and Topologies. Technical Report March, National Renewable Energy Laboratory, 2008.
- [4] Qiang Li, Michele Lim, Julu Sun, Arthur Ball, Yucheng Ying, Fred C Lee, and K D T Ngo. Technology Road Map for High Frequency Integrated DC-DC Converter. In Twenty-Fifth Annual IEEE Applied Power Electronics Conference and Exposition (APEC), pages 533–539, 2010.
- [5] M. Schaefer, et al., “Magnetic Losses in Ferrites and Nanocrystalline Ribbons for Power Applications”, *J. Magn. Magn. Mater.* 101 (1-3), (1991), 95-96.
- [6] R. Hasegawa, “Applications of Amorphous Magnetic Alloys in Electronic Devices”, *J.Non-Cryst. Solids* 287 (1-3), (2001), 405-412. 280
- [7] R. Hasegawa, “Applications of Amorphous Magnetic Alloys”, *Mater. Sci. Eng., A* 375-377, (2004), 90-97.
- [8] EIA. Net Generation by Energy Source: Total (All Sectors), 2003-March 2013. Retrieved April 6, 2013
- [9] D.O.E. Power Electronics Research and Development Program Plan. Retrieved April 6, 2013, from http://energy.gov/sites/prod/files/oeprod/DocumentsandMedia/OE_Power_Electronics_Program_Plan_April_2011.pdf
- [10] Rectifiers, H. S., Yoshida, T., Shiizuka, O., Miyashita, O., & Ohniwa, K. (2000). An Improvement Technique for the Efficiency of, *IS*(6), 1118–1123.

- [11] Long, J., McHenry, M., Urciuoli, D. P., Keylin, V., Huth, J., & Salem, T. E. (2008). Nanocrystalline material development for high-power inductors. *Journal of Applied Physics*, 103(7)
- [12] McHenry, M. E. (2012). Nanocomposite Alloy Design for High Frequency Power Converter Applications, 275–282.
- [13] M. E. McHenry, M. A. Willard and D. E. Laughlin, “Amorphous and Nanocrystalline Materials for Applications as Soft Magnets”, *Prog. Mater Sci.* 44 (4), (1999), 291-433.
- [14] Nikolov, G. T., & Valchev, V. C. (2009). Nanocrystalline magnetic materials versus ferrites in power electronics. *Procedia Earth and Planetary Science*, 1(1), 1357–1361.
- [15] Binkofski, J. (n.d.). Influence of the properties of magnetic materials on the size and performance of PLC couplers., 5–8.
- [16] William, C. T. M. (2004). *Transformer and Inductor Design Handbook* (pp. 1–27 to 1–28). CRC Press.
- [17] http://www.eia.gov/electricity/monthly/epm_table_grapher.cfm?t=epmt_1_1
- [18] D.O.E. Power Electronics Research and Development Program. Retrieved April 6, 2013, from http://energy.gov/sites/prod/files/oeprod/DocumentsandMedia/OE_Power_Electronics_Program_Plan_April_2011.pdf
- [19] Muhlethaler, J., Biela, J., Kolar, J. W., & Ecklebe, a. (2010). Core losses under DC bias condition based on Steinmetz parameters. *The 2010 International Power Electronics Conference - ECCE ASIA* -, 2430–2437.
- [20] Hyperphysics. Retrieved from <http://hyperphysics.phystr.gsu.edu/hbase/magnetic/indtor.html>
- [21] Maxwell 2D Technical Notes > 2D Sources/Excitations > 2D Current/Current Density ANSYS Maxwell Help Manual.
- [22] University, D. Skin Effect, Proximity Effect, and Litz Wire. Retrieved from <http://www.dartmouth.edu/~sullivan/litzwire/skin.html>
- [23] Assigning New Materials > Adding New Materials. ANSYS Maxwell Help Manual.
- [24] Assigning Materials > Calculating Properties for Core Loss (BP Curve). ANSYS Maxwell Help Manual.
- [25] Software, D., & Components, M. PExprt.

- [26] Prieto, R., Oliver, J. A., Cobos, J. a., Uceda, J., & Christini, M. (1999). Errors obtained when 1D magnetic component models are not properly applied. *APEC '99. Fourteenth Annual Applied Power Electronics Conference and Exposition. 1999 Conference Proceedings (Cat. No.99CH36285)*, 206–212 vol.1.
- [27] Asensi, R., Cobos, J. A., Prieto, R., Uceda, J., & Abascal, G. (1994). A Full Procedure to Model High Frequency Transformer Windings, (Esprit 6484).
- [28] Prieto, R., Asensi, R., Cobos, J. a., & Uceda, J. (2004). A full procedure to model integrated magnetics based on FEA. *Nineteenth Annual IEEE Applied Power Electronics Conference and Exposition, 2004. APEC '04.*, 2, 952–957.
- [29] EPRI. "DC Power Production, Delivery and Utilization." *EPRI*. Web. <http://mydocs.epri.com/docs/CorporateDocuments/WhitePapers/EPRI_DCpower_June2006.pdf>.
- [30] Ericson, T., "The ship power electronic revolution: Issues and answers," *Petroleum and Chemical Industry Technical Conference, 2008. PCIC 2008. 55th IEEE* , vol., no., pp.1-11, 22-24 Sept. 2008
- [31] Woodford, Dennis, A., "Basic Principles of HVDC" *Manitoba HVDC Research Centre*. Web. <<https://pscad.com/resource/File/Library/BasisPrinciplesofHVDC.pdf>>.
- [32] Chapman, S. J. (2005). *Electric Machinery Fundamentals* (pp. 380 – 444).
- [33] Dems, M., & Komez, K. (2012). Performance characteristics of a high-speed energy-saving induction motor with an amorphous stator core. *2012 XXth International Conference on Electrical Machines*, 2454–2461.
- [34] European Steel and Alloy Grades - M600-50A. Retrieved from http://www.steelnumber.com/en/steel_composition_eu.php?name_id=1933
- [35] Typical Data for SURA M600-50A. Retrieved from [http://www.sura.se/Sura/hp_products.nsf/vOpenDocument/03A8B2433FAE16C4C1256AA8002280E6/\\$FILE/600-50.pdf?OpenElement](http://www.sura.se/Sura/hp_products.nsf/vOpenDocument/03A8B2433FAE16C4C1256AA8002280E6/$FILE/600-50.pdf?OpenElement)
- [36] Melfi, M. J. Optimum pole configuration of AC induction motors used on adjustable frequency power supplies. *Industry Applications Society 42nd Annual Petroleum and Chemical Industry Conference*, 237–242. doi:10.1109/PCICON.1995.523959
- [37] Honsinger, V. B. (1987). Sizing Equations for Electrical Machinery, (1), 116–121.
- [38] Matsch, L. W. (1954). Capacitors, Magnetic Circuits and Transformers. Retrieved from http://www.vias.org/matsch_capmag/matsch_caps_magnetics_chap5_02.html